



1 **Constraining N<sub>2</sub>O emissions since 1940 using firn air isotope measurements in**  
2 **both hemispheres**

3 **M. Prokopiou<sup>1</sup>, P. Martinerie<sup>2</sup>, C. J. Sapart<sup>1,3</sup>, E. Witrant<sup>4</sup>, G. A. Monteil<sup>1,5</sup>, K.**  
4 **Ishijima<sup>6</sup>, S. Bernard<sup>2</sup>, J. Kaiser<sup>7</sup>, I. Levin<sup>8</sup>, T. Sowers<sup>9</sup>, T. Blunier<sup>10</sup>, D.**  
5 **Etheridge<sup>11</sup>, E. Dlugokencky<sup>12</sup>, R. S. W. van de Wal<sup>1</sup>, T. Röckmann<sup>1</sup>**

6 <sup>1</sup> Institute for Marine and Atmospheric research Utrecht, Utrecht, The Netherlands

7 <sup>2</sup> University of Grenoble Alpes/CNRS, LGGE, F-38000 Grenoble, France

8 <sup>3</sup> Laboratoire de Glaciologie, ULB, Brussels, Belgium

9 <sup>4</sup> University of Grenoble Alpes/CNRS, GIPSA-Lab, F-38000 Grenoble, France

10 <sup>5</sup> Department of Physical Geography and Ecosystem Science, Lund University, Lund, Sweden

11 <sup>6</sup> National Institute of Polar Research, Tokyo, Japan

12 <sup>7</sup> Centre for Ocean and Atmospheric Sciences, School of Environmental Sciences, University  
13 of East Anglia, Norwich, United Kingdom

14 <sup>8</sup> Institute of Environmental Physics, Heidelberg University, Germany

15 <sup>9</sup> Earth and Environmental Systems Institute, Pennsylvania, USA

16 <sup>10</sup> Centre for Ice and Climate, Niels Bohr Institute, Copenhagen, Denmark

17 <sup>11</sup> CSIRO Marine and Atmospheric Research, Victoria, Australia

18 <sup>12</sup> NOAA Earth System Research Laboratory, Boulder, Colorado, USA

19 **Abstract**

20 N<sub>2</sub>O is currently the 3<sup>rd</sup> most important anthropogenic greenhouse gas in terms of radiative  
21 forcing and its atmospheric mole fraction is rising steadily. To quantify the growth rate and its  
22 causes, we performed a multi-site reconstruction of the atmospheric N<sub>2</sub>O mole fraction and  
23 isotopic composition using firn air data collected from Greenland and Antarctica in  
24 combination with a firn diffusion and densification model. The multi-site reconstruction  
25 showed that while the global mean N<sub>2</sub>O mole fraction increased from (290±1) nmol mol<sup>-1</sup> in  
26 1940 to (322±1) nmol mol<sup>-1</sup> in 2008 the isotopic delta [values] of atmospheric N<sub>2</sub>O decreased  
27 by (−2.2±0.2) ‰ for δ<sup>15</sup>N<sup>av</sup>, (−1.0±0.3) ‰ for δ<sup>18</sup>O, (−1.3±0.6) ‰ for δ<sup>15</sup>N<sup>α</sup>, and (−2.8±0.6)  
28 ‰ for δ<sup>15</sup>N<sup>β</sup> over the same period. The detailed temporal evolution of the mole fraction and



isotopic composition derived from the firm air model was then used in a two-box atmospheric model (comprising a stratospheric and a tropospheric box) to infer changes in the isotopic source signature over time. The precise value of the source strength depends on the choice of the  $\text{N}_2\text{O}$  lifetime, which we choose to be  $123^{+29}_{-19}$  a. Adopting this lifetime results in total average source isotopic signatures of  $(-7.6 \pm 0.8) \text{‰}$  (vs. Air- $\text{N}_2$ ) for  $\delta^{15}\text{N}^{\text{av}}$ ,  $(32.2 \pm 0.2) \text{‰}$  (vs. VSMOW) for  $\delta^{18}\text{O}$ ,  $(-3.0 \pm 1.9) \text{‰}$  (vs. Air- $\text{N}_2$ ) for  $\delta^{15}\text{N}^{\alpha}$ , and  $(-11.7 \pm 2.3) \text{‰}$  (vs. Air- $\text{N}_2$ ) for  $\delta^{15}\text{N}^{\beta}$  over the investigated period.  $\delta^{15}\text{N}^{\text{av}}$  and  $\delta^{15}\text{N}^{\beta}$  show some temporal variability while the other source isotopic signatures remain unchanged. The  $^{15}\text{N}$  site-preference ( $= \delta^{15}\text{N}^{\alpha} - \delta^{15}\text{N}^{\beta}$ ) can be used to reveal further information on the source emission origins. Based on the changes in the isotopes we conclude that the main contribution to  $\text{N}_2\text{O}$  changes in the atmosphere since 1940 is from soils, with agricultural soils being the principal anthropogenic component which is in line with previous studies.

## 1 Introduction

The rise of nitrous oxide ( $\text{N}_2\text{O}$ ) since pre-industrial times contributes significantly to radiative forcing (Forster et al., 2007). Over the past four decades, the  $\text{N}_2\text{O}$  mole fraction has increased by 0.25 % per year, reaching  $324 \text{ nmol mol}^{-1}$  in 2011 (IPCC, ch.6, 2013). Therefore, the understanding of the biogeochemical cycle of  $\text{N}_2\text{O}$  is important for a reliable assessment of future climate change. In addition, the destruction of  $\text{N}_2\text{O}$  in the stratosphere provides an important source of nitrogen oxides ( $\text{NO}_x$ ), which contribute to stratospheric ozone depletion (Ravishankara et al., 2009).

Natural sources of  $\text{N}_2\text{O}$  are microbial processes in soils and oceans, which produce  $\text{N}_2\text{O}$  during nitrification and denitrification (Bouwman et al., 2013; Loescher et al., 2012; Santoro et al., 2011; Galloway et al., 2004; Pérez et al., 2001; Yung and Miller, 1997; Kim and Craig, 1993). The increase of  $\text{N}_2\text{O}$  since pre-industrial times (hereafter referred to as "anthropogenic" increase) has been attributed largely to increased microbial production, resulting from the increased use of nitrogen fertilizers in agriculture. Industry (especially nylon production) and fossil fuel combustion present a smaller contribution to the anthropogenic source (Davidson, 2009; Kroeze et al., 1999; Mosier et al., 1998).  $\text{N}_2\text{O}$  is primarily destroyed in the stratosphere via UV photolysis (90%) and reactions with excited oxygen atoms (10 %) (Minschwaner et al., 1993), with a minor  $\text{N}_2\text{O}$  fraction removed by surface sinks (Syakila, 2010).



60 Estimates of the total  $\text{N}_2\text{O}$  source strength from various bottom-up and top-down studies  
61 suggest a mean value of roughly  $17 \text{ Tg a}^{-1} \text{ N}$  equivalents at present. However, the range in  
62 both approaches is large, especially for bottom-up estimates, which range between 8.5 and  
63  $27.7 \text{ Tg a}^{-1} \text{ N}$ , whereas top-down estimates range between 15.8 and  $18.4 \text{ Tg a}^{-1} \text{ N}$  (Potter et  
64 al., 2011 and references therein). Besides the total source strength, the contributions of  
65 individual source processes are also poorly constrained. Due to the long steady-state lifetime  
66 of  $\text{N}_2\text{O}$  in the atmosphere ( $123_{-19}^{+29} \text{ a}$ ; SPARC Lifetimes Report 2013), temporal and spatial  
67 gradients are small, making it difficult to resolve localised sources.

68 Measurements of the isotopic composition of  $\text{N}_2\text{O}$  may help to constrain the atmospheric  $\text{N}_2\text{O}$   
69 budget. The  $\text{N}_2\text{O}$  molecule is linear (NNO) and the two N atoms are chemically  
70 distinguishable; thus they tend to attain different isotopic compositions. Beyond oxygen  
71 ( $\delta^{18}\text{O}$ ,  $\delta^{17}\text{O}$ ) and average  $\delta^{15}\text{N}^{\text{av}}$  ("bulk") signatures,  $\text{N}_2\text{O}$  also displays site specific  $^{15}\text{N}$   
72 isotopic information. Site preference ( $\delta^{15}\text{N}^{\text{sp}}$ ) is defined as the difference in  $\delta^{15}\text{N}$  between the  
73 central (2,  $\mu$  or  $\alpha$ ) and terminal position (1,  $\tau$  or  $\beta$ ) of N atoms in  $\text{N}_2\text{O}$  (Kaiser, 2002;  
74 Brenninkmeijer and Röckmann, 2000; Yoshida and Toyoda, 1999),  
75 i.e.  $\delta^{15}\text{N}^{\text{sp}} = \delta^{15}\text{N}^{\alpha} - \delta^{15}\text{N}^{\beta}$ . For consistency with many recent publications in the field, we here  
76 adopt the nomenclature from Yoshida and Toyoda (1999),  $\alpha$  and  $\beta$ , for the two positions.

77 The different sources and sinks of  $\text{N}_2\text{O}$  are associated with characteristic fractionation  
78 processes leading to different isotope ratios. For example, microbial sources emit  $\text{N}_2\text{O}$  that is  
79 depleted in  $^{15}\text{N}$  and  $^{18}\text{O}$  relative to the tropospheric background.  $\text{N}_2\text{O}$  that returns from the  
80 stratosphere after partial photochemical removal is enriched in both heavy isotopes (Yoshida  
81 and Toyoda, 2000; Yung and Miller, 1997; Kim & Craig, 1993). Stratospheric  $\text{N}_2\text{O}$  also has a  
82 high  $^{15}\text{N}$  site-preference compared to tropospheric  $\text{N}_2\text{O}$ . The observed enrichment is caused  
83 by kinetic isotope fractionation in the stratospheric sink reactions (Kaiser et al., 2006; 2002;  
84 Park et al., 2004; Röckmann et al., 2001; Yoshida and Toyoda, 2000).

85 The multi-isotope signature of  $\text{N}_2\text{O}$  adds useful constraints on its budget. In particular, when  
86 the isotopic composition of tropospheric  $\text{N}_2\text{O}$  is combined with the fractionation during its  
87 removal in the stratosphere, the isotopic composition of the global average source can be  
88 determined (Ishijima et al., 2007; Bernard et al., 2006; Röckmann et al., 2003; Kim and Craig,  
89 1993).

90 The temporal variations of the  $\text{N}_2\text{O}$  isotopic composition are difficult to quantify on a short  
91 timescale because of its long residence time in the atmosphere. Longer time scales can be



92 reconstructed by using air trapped in Arctic and Antarctic firn and ice which provides a  
93 natural archive of past atmospheric composition. The firn phase is the intermediate stage  
94 between snow and glacial ice, which constitutes the upper 40-120 m of the accumulation zone  
95 of ice sheets. Within the firn, air exchanges relatively freely in the upper layers and with the  
96 overlying atmosphere (convective zone). With increasing depth the air pores shrink in size  
97 due to firn compaction, and air mixes primarily via slow diffusion in the diffusive zone. At  
98 densities larger than  $\approx 815 \text{ kg m}^{-3}$ , air is permanently trapped in closed bubbles in the ice and  
99 totally isolated from the atmosphere. The precise age range of air that can be retrieved from  
100 polar firn between the surface and bubble close-off depends on site specific characteristics  
101 like temperature, accumulation rate and porosity and typically ranges from several decades to  
102 120 years.

103 For  $\text{N}_2\text{O}$ , a number of studies have reported isotope measurements from different Arctic and  
104 Antarctic firn drilling sites showing a steady decrease of the heavy isotope content of  $\text{N}_2\text{O}$   
105 over the past decades (Park et al., 2012; Ishijima et al., 2007; Bernard et al., 2006; Röckmann  
106 et al., 2003; Sowers et al., 2002). A more recent study by Park et al. (2012) attempted to  
107 reconstruct the long-term trends in  $\text{N}_2\text{O}$  isotopic compositions and its seasonal cycles to  
108 further distinguish between the influence of the stratospheric sink and the oceanic source at  
109 Cape Grim, Tasmania, demonstrating that isotope measurements can help in the attribution  
110 and quantification of surface sources in general.

111 Taking into account the long atmospheric lifetime of  $\text{N}_2\text{O}$  and the fact that both hemispheres  
112 are well mixed on annual timescales, it is reasonable to assume that the results from these  
113 studies are representative for the global scale. However care needs to be taken because small  
114 differences in the diffusivity profiles of the firn column lead to large effect on the isotope  
115 signature (Buizert et al. 2012). Interestingly, for atmospheric methane ( $\text{CH}_4$ ), another  
116 important greenhouse gas, a recent multi-site analysis on the carbon isotopic composition of  
117 showed large differences among reconstructions from different sites (Sapart et al., 2013). In  
118 particular, firn fractionation effects related to diffusion and gravitational separation and their  
119 implementation in models (Buizert et al., 2012) have large effects on the reconstructed  
120 signals. Small differences in the diffusivity profiles of the firn column lead to large effects on  
121 the isotope signatures. Therefore, more robust results may be obtained by combining isotope  
122 information from a number of different sites in a multi-site reconstruction, including a critical  
123 evaluation of diffusivity profiles.



Here we combine new  $\text{N}_2\text{O}$  isotope measurements from the NEEM site in Greenland with previously published firn air  $\text{N}_2\text{O}$  isotope records from 4 different sites from Greenland and Antarctica to reconstruct records of the  $\text{N}_2\text{O}$  isotopic composition over the last 70 years. We use the multi-gas firn transport model established by the Laboratoire de Glaciologie et Géophysique de l'Environnement and Grenoble Image Parole Signal Automatique (LGGE-GIPSA) to obtain an atmospheric scenario that is constrained by and consistent with all individual sites (Allin et al., 2015; Witrant et al., 2012; Wang et al., 2012; Rommelaere et al., 1997). We then use an isotope mass balance model to infer the changes in the isotopic signature of the  $\text{N}_2\text{O}$  source over time to investigate possible changes in the source mix.

## 2 Materials and Methods

### 2.1 Firn air Sampling

New firn air samples added in this study to the total dataset were collected in 2008 and 2009 during the firn campaign (Buizert et al., 2011) as part of the North Eemian Ice Drilling programme (NEEM) in Greenland ( $77.45^\circ \text{ N } 51.06^\circ \text{ W}$ ). These data are combined with existing firn air data from four other sites. Information on the locations is provided in Table 1. The firn air collection procedure is described in detail by Schwander et al. (1993). Here a brief description is presented. Essentially a borehole is drilled in the firn to a certain depth and then the firn air sampling device is inserted into the borehole. The device consists of a bladder, a purge line and a sample line. When the sampling device reaches the desired depth the bladder is inflated to seal the firn hole and isolate the air below the bladder from the overlying atmosphere, and air is pumped out from the pore space below the bladder. Continuous online  $\text{CO}_2$  concentration measurements are performed to verify that no contamination with contemporary air occurs during the extraction procedure. After the contaminating air has been pumped away, firn air is collected in stainless steel, glass or aluminium containers.

### 2.2 $\text{N}_2\text{O}$ isotope analysis

The firn air samples from NEEM are analyzed for  $\text{N}_2\text{O}$  isotopocules at the Institute for Marine and Atmospheric research Utrecht (IMAU). The  $\text{N}_2\text{O}$  mole fraction and isotopic composition are measured using continuous flow isotope ratio mass spectrometry (IRMS). The method is described in detail by Röckmann et al. (2003b). Here only a brief summary is



given. The firm air sample (333 mL) is introduced into the analytical system at a flow rate of 50 mL/min for 400 s. After CO<sub>2</sub> is removed chemically over Ascarite, N<sub>2</sub>O and other condensable substances are cryogenically preconcentrated. After cryo-focusing the sample the remaining traces of CO<sub>2</sub> and other contaminants are removed on a capillary GC column (PoraPlot Q, 0.32 mm i.d., 25 m). The column is separated into a pre-column and an analytical column. This set-up eliminates interferences from other atmospheric compounds that have much longer retention times. Finally the sample is transferred to the IRMS via an open split interface. For the new NEEM samples reported here, each firm air sample has been measured five times. Before and after each sample we measured five aliquots of air from a reference cylinder with known isotopic composition and mole fraction for calibration purposes.

$\delta^{15}\text{N}$  values are reported with respect to Air-N<sub>2</sub> while  $\delta^{18}\text{O}$  refers to Vienna Standard Mean Ocean Water (VSMOW). As laboratory reference gas we used an atmospheric air sample with an N<sub>2</sub>O mole fraction of 318 nmol mol<sup>-1</sup> and  $\delta$  values of (6.4±0.2) ‰ for  $\delta^{15}\text{N}^{\text{av}}$  vs. Air-N<sub>2</sub>, (44.9±0.4) ‰ for  $\delta^{18}\text{O}$  vs. VSMOW. The intramolecular  $\delta^{15}\text{N}^{\text{av}}$  values of the air standard are  $\delta^{15}\text{N}^{\alpha} = (15.4\pm1.2)$  ‰ and  $\delta^{15}\text{N}^{\beta} = (-2.7\pm1.2)$  ‰. The calibration of the intramolecular distribution follows Toyoda and Yoshida (1999). Typically the 1 $\sigma$  standard deviation of replicate sample measurements are 0.1 ‰ for  $\delta^{15}\text{N}$ , 0.2 ‰ for  $\delta^{18}\text{O}$  and 0.3 ‰ for  $\delta^{15}\text{N}^{\alpha}$  and  $\delta^{15}\text{N}^{\beta}$ .

### 2.3 Modelling trace gas transport in firm

In firm air, the interstitial gas is not yet isolated in closed-off bubbles, so diffusion processes and gravitational separation alter mole fractions and isotope ratios over time. Thus, firm air measurements cannot be used directly to derive the atmospheric history of trace gas signatures. Over time, atmospheric compositional changes are propagated downwards into the firm based on the diffusivity of the atmospheric constituent in question. Firm air diffusion models take these effects into account and thereby allow reconstruction of changes in the atmospheric composition from the firm profile.

In this study we use the LGGE-GIPSA firm air transport model to reconstruct the temporal evolution of N<sub>2</sub>O mole fraction and isotopic composition from the measured firm profiles (Allis et al., 2015; Witrant et al., 2012; Wang et al., 2012; Rommelaere et al., 1997).



184 In the “forward version” of LGGE-GIPSA, a physical transport model uses a historic  
185 evolution of atmospheric N<sub>2</sub>O mole fractions to calculate the vertical profiles of mole  
186 fractions in firn. For the isotopocules, further simulations are performed separately to  
187 calculate their respective vertical profiles. Important parameters needed to constrain the  
188 model are the site temperature, accumulation rate, depth of the convective layer and close-off  
189 depth, together with profiles of firn density and effective diffusivity. The latter parameter is  
190 determined as a function of depth for each firn-drilling site by modelling the mole fractions in  
191 firn for trace gases with well known atmospheric histories (Buizert et al., 2012; Witrant et al.,  
192 2012; Rommelaere et al., 1997; Trudinger et al., 1997). A multi-gas constrained inverse  
193 method (Witrant et al., 2012) is used to calculate the effective diffusivity of each site for each  
194 specific gas. It is noteworthy that diffusivity is not constrained equally well at all sites  
195 because different sets of constraints (e.g. number of available reference gases) are used at  
196 different sites and because of different depth resolutions.

197 A Green-function approach as presented by Rommelaere et al. (1997), with an extension for  
198 isotopic ratios and revised to take into account the sparsity of the measurements (Witrant and  
199 Martinerie, 2013; Martinerie et al., 2012; Wang et al., 2011) is used to assign a mean age and  
200 age distribution to a certain depth.

201 Due to the long N<sub>2</sub>O residence time in the atmosphere, the global variability of the isotopic  
202 composition of N<sub>2</sub>O is very small and no significant variations between individual  
203 background locations have been detected so far (Kaiser et al., 2003). In particular, the isotope  
204 ratio difference between northern and southern hemisphere tropospheric air is expected to be  
205 only −0.06 ‰ (based on an interhemispheric mole fraction gradient of 1.2 nmol mol<sup>−1</sup> [Hirsch  
206 et al. 2006] and isotope ratio difference of −15 ‰ between average source and average  
207 tropospheric isotope delta). These differences are within the uncertainties of the firn air  
208 measurements used here and therefore the data from the northern and southern hemisphere are  
209 combined into a single dataset without including an interhemispheric gradient.

210 With the multi-site reconstruction method, we used the measurements from six firn air  
211 drillings at five sites (NEEM-09, NEEM-EU-08, NGRIP-01, BKN-03, DC-99, DML-98) to  
212 constrain our model and determine a set of atmospheric reconstructions that fits all sites. Data  
213 from Ishijima et al. (2007) and Sowers et al. (2002) [NGRIP-01 and SP-01, SP-95  
214 respectively] were not included in our multi-site reconstruction because no data for  $\delta^{15}\text{N}^a$  and



215  $\delta^{15}\text{N}^{\beta}$  were published for those sites. These datasets were used for independent validation of  
216  $\delta^{15}\text{N}^{\text{av}}$  and  $\delta^{18}\text{O}$ .

217 To quantify the isotope fractionation due to diffusion and gravitational settling within the firn,  
218 a forward firn transport model simulation was carried out with a realistic  $\text{N}_2\text{O}$  mole fraction  
219 scenario (based on the Law Dome record, MacFarling Meure et al., 2001), but with a constant  
220 isotopic  $\text{N}_2\text{O}$  history. This allows determining the role of transport isotope fractionation  
221 occurring in the firn, in the absence of isotopic changes in the atmosphere. The results are  
222 used to subtract the firn fractionation effects from the measured signals, which can then be  
223 used to assess the atmospheric history. Compared to the signal, the effect of firn fractionation  
224 is minor for  $\delta^{15}\text{N}$ , but important for  $\delta^{18}\text{O}$  especially at the lower accumulation rates in the  
225 Southern Hemisphere (see Appendix A).

226 The deepest firn data from each site provide constraints furthest back in time and the oldest  
227 air samples that are included in the inversion are from the DML-98 and DC-99, which extend  
228 the reconstruction of atmospheric  $\text{N}_2\text{O}$  back to the early 20<sup>th</sup> century (Röckmann et al., 2003).  
229 At the same, the correction for isotopic fractionation in firn is most uncertain for the deepest  
230 samples, where strong differences between individual firn air models have been reported  
231 (Buizert et al., 2012).

## 232 **2.4 Scaling of different data sets**

233 At present, no international reference materials for the isotopic composition of  $\text{N}_2\text{O}$  exist.  
234 Kaiser et al. (2003) and Toyoda et al. (1999) linked the isotopic composition of  $\text{N}_2\text{O}$  in  
235 tropospheric air to the international isotopes scales for nitrogen isotopes ( $\text{Air-N}_2$ ) and oxygen  
236 isotopes (either VSMOW or  $\text{Air-O}_2$ ). Our measurements are linked to a standard gas cylinder  
237 of tropospheric air with known  $\text{N}_2\text{O}$  mole fraction and isotopic composition based on the  
238 scale of Kaiser et al. (2003) for  $\delta^{15}\text{N}^{\text{av}}$  and  $\delta^{18}\text{O}$  values and Yoshida and Toyoda (1999) for  
239 position dependent  $^{15}\text{N}$  values. However, the reference air cylinder used for the calibration  
240 was exhausted and had to be replaced three times over the years in which the different  
241 measurement that we combine in this study were performed. Although the cylinders were  
242 carefully compared, the long-time consistency of the isotope scale could not be guaranteed  
243 because long-time isotope standards are not available. In fact, analysis of the data from the  
244 convective zone for the different sites, show small but significant differences from the  
245 temporal trends that are well established from previously published data from the German





246 Antarctic Georg von Neumayer station for 1990 to 2002 (Röckmann and Levin; 2005). The  
247 linear trends reported in that paper are  $(-0.040 \pm 0.003) \text{‰ a}^{-1}$  for  $\delta^{15}\text{N}^{\text{av}}$ ,  $(0.014 \pm 0.016) \text{‰ a}^{-1}$   
248 for  $\delta^{15}\text{N}^{\alpha}$ ,  $(-0.064 \pm 0.016) \text{‰ a}^{-1}$  for  $\delta^{15}\text{N}^{\beta}$  and  $(-0.021 \pm 0.003) \text{‰ a}^{-1}$  for  $\delta^{18}\text{O}$ . Since they were  
249 derived from direct air samples (unaffected by firn fractionation), these trends can be used as  
250 a reference to re-scale the different firn air results from different dates. To do so, data from  
251 the diffusive zone ( $\rho < 815 \text{ kg m}^{-3}$ ) for each individual site were scaled to one reference site,  
252 DC-99, taking into account the temporal differences in sampling and the model-assigned  
253 mean age of the firn air samples (see below). DC-99 was chosen as reference site because it  
254 has most measurements in the diffusive zone. Also, the precision of these measurements was  
255 high because high volume cylinders were available from which many measurements could be  
256 performed and averaged. To test the sensitivity to the choice of reference site, we repeated the  
257 re-scaling using NEEM-09 as reference, which generated almost identical results within  
258 uncertainty bars (Appendix C).

259 The average difference between the samples from the diffusive zone at a given site and the  
260 interpolated DC-99 results was compared to the expected temporal trend between the  
261 sampling date of each station and DC-99, using the temporal trends established by Röckmann  
262 and Levin (2005), as shown in the equations below. The effect of this scaling is that the  
263 temporal trend in the past decade is effectively forced to follow the atmospheric  
264 measurements at Neumayer station (Röckmann and Levin, 2005).

265 After re-scaling the firn isotopic data we detected some individual data points that clearly  
266 deviated from the general trends. These were considered outliers, because they exceeded the  
267  $2\sigma$  error, and were removed from the dataset. All of these values are site-specific  $^{15}\text{N}$  values,  
268 specifically, the following, were excluded: NEEM-EU-08 hole depth  $-4.9 \text{ m}$ ,  $-34.72 \text{ m}$ ,  $-$   
269  $61.95 \text{ m}$  and  $-74.5 \text{ m}$ , and NEEM-09 hole depth  $1.0 \text{ m}$ ,  $0.2 \text{ m}$  and  $-69.4 \text{ m}$ .

270 The mole fraction data that can be obtained from the NEEM air isotope measurements were  
271 substituted with more precise measurements of  $\text{N}_2\text{O}$  mole fraction by the Commonwealth  
272 Scientific and Industrial Research Organisation (CSIRO) the Institute of Environmental  
273 Physics, University of Heidelberg (IUP), the Centre of Ice and Climate, University of  
274 Copenhagen (CIC) and National Oceanic and Atmospheric Administration (NOAA). In this  
275 way we combine all available  $\text{N}_2\text{O}$  mole fraction data.

276 The mole fraction data were scaled to the most recent international scale, NOAA-2006A from  
277 the CSIRO scale or the NOAA-2000 scale. Conversion of the NOAA-2000 data to the



NOAA-2006A scale is done using a conversion factor available by National Oceanic and Atmospheric Administration (NOAA) ([http://www.esrl.noaa.gov/gmd/cc/cales/N2O\\_scale.html](http://www.esrl.noaa.gov/gmd/cc/cales/N2O_scale.html)). Converting from the CSIRO to the NOAA-2006A scale, though, requires the reference cylinder details, which were not available. Instead we used a trend scenario, based on the CSIRO atmospheric scale combined with Law Dome data and assuming a constant interhemispheric gradient. This trend scenario was then compared with the data provided on NOAA-2006A scale, and a polynomial fit was generated, which was then used to convert the data to the NOAA-2006A scale. All results presented in the next section are based on the scaling procedure and removal of the outliers as described above (Appendix B).

## 2.5 Global N<sub>2</sub>O (isotope) budget calculations

The tropospheric budget is controlled by N<sub>2</sub>O emissions from natural and anthropogenic sources at the surface and by the exchange between troposphere and stratosphere. A simple two-box model is used to quantitatively understand the emissions and the budget changes of N<sub>2</sub>O. The model consists of a tropospheric N<sub>2</sub>O reservoir (index T) into which N<sub>2</sub>O is emitted from natural (E<sub>nat</sub>) and anthropogenic (E<sub>anth</sub>) sources. N<sub>2</sub>O is then transported to the stratosphere (index S) where part of it is destroyed by photochemical reactions (F<sub>sink</sub>), and the remainder returns from the stratosphere to the troposphere (TS<sub>exch</sub>).

The change in the tropospheric N<sub>2</sub>O reservoir is given by the following mass balance equations (Allin et al, 2015):

$$n_T \frac{d\chi_T}{dt} = E_{\text{nat}} + E_{\text{anth}} - F_{\text{exch}}(\chi_T - \chi_S) \quad (1)$$

$$n_S \frac{d\chi_S}{dt} = F_{\text{exch}}(\chi_T - \chi_S) - L \quad (2)$$

where  $n$  is the amount of air and  $\chi_S$  and  $\chi_T$  are the mole fractions of N<sub>2</sub>O in the stratosphere and troposphere respectively. Annual fluxes between the two reservoirs,  $F_{\text{exch}}$ , are calculated based on previous estimates (Appenzeller et al., 1996; Holton et al., 1990). The loss due to stratospheric sink is determined by:

$$L = \frac{n_T \chi_T + n_S \chi_S}{\tau} \quad (3)$$

where  $\tau$  is the atmospheric lifetime of  $123^{+29}_{-19}$  a.



306 The isotopic budgets are calculated by simply multiplying the reservoir sizes with the  
 307 corresponding  $\delta$  values of the different flux terms:

$$308 \quad n_T \frac{d\chi_T \delta_T}{dt} = E_{\text{nat}} \delta_{\text{nat}} + E_{\text{anth}} \delta_{\text{anth}} + F_{\text{exch}} (\chi_S \delta_S - \chi_T \delta_T) \quad (4)$$

$$309 \quad n_S \frac{d\chi_S \delta_S}{dt} = F_{\text{exch}} (\chi_T \delta_T - \chi_S \delta_S) - L \delta_L \quad (5)$$

310 Solving equations 4 and 5 and substituting equations 1 and 2 we reach the final isotope  
 311 equations:

$$312 \quad n_T \frac{d\delta_T}{dt} = \frac{E_{\text{nat}}}{\chi_T} (\delta_{\text{nat}} - \delta_T) + \frac{E_{\text{anth}}}{\chi_T} (\delta_{\text{anth}} - \delta_T) + \frac{F_{\text{exch}} \chi_S}{\chi_T} (\delta_S - \delta_T) \quad (6)$$

$$313 \quad n_S \frac{d\delta_S}{dt} = \frac{F_{\text{exch}} \chi_T}{\chi_S} (\delta_T - \delta_S) - \frac{L}{\chi_S} \varepsilon_L \quad (7)$$

314 where  $\delta_T$  is either  $\delta^{15}\text{N}^{\text{av}}$ ,  $\delta^{18}\text{O}$ ,  $\delta^{15}\text{N}^{\alpha}$ ,  $\delta^{15}\text{N}^{\beta}$  from the multi-site reconstruction as shown  
 315 below.  $\delta_{\text{nat}}$  and  $\delta_{\text{anth}}$  is the isotopic composition of the natural and anthropogenic  $\text{N}_2\text{O}$  source,  
 316 respectively (our target quantity).  $\varepsilon_L$  is the apparent fractionation factor associated with  
 317 stratospheric destruction.

318  $\delta_S$  is also not known in this case, but can be calculated using the analogue from Röckmann et  
 319 al. (2003) by employing the observed apparent Rayleigh fractionation in the stratosphere  
 320 ( $\varepsilon_{\text{app}}$ ). Based on this, the relative isotope ratio difference between the stratosphere and the  
 321 troposphere can be calculated by:

$$322 \quad \delta_S = \left[ (\delta_T + 1) \left( \frac{\chi_S}{\chi_T} \right)^{\varepsilon_{\text{app}}} - 1 \right] \quad (8)$$

323 where  $\varepsilon_{\text{app}}$  represents the stratospheric fractionation constant associated with this removal  
 324 process. Here, we used the average  $\varepsilon_{\text{app}}$  of all lowermost stratospheric measurements from  
 325 Kaiser et al. (2006) (Table 3). Note that slightly different fractionations  $\varepsilon_{\text{app}}$  have been used  
 326 in previous studies by Röckmann (2001) and Park et al. (2012; 2004) and the sensitivity to  
 327 these differences will be examined below.

328 Furthermore we assume that the  $\text{N}_2\text{O}$  lifetime and  $\varepsilon_{\text{app}}$  remained constant from pre-industrial  
 329 time to 2008, thus the annual strength removal can be scaled down from its current value at  
 330  $\chi_T = 322 \text{ nmol mol}^{-1}$  to the pre-industrial level of  $\chi_{T,\text{pi}} = 270 \text{ nmol mol}^{-1}$  and the relative



331 enrichment of stratospheric N<sub>2</sub>O relative to tropospheric N<sub>2</sub>O described by Eq. 8 remains  
 332 constant over time. The effect of changing the N<sub>2</sub>O lifetime is examined below.

333 Furthermore it is hypothesized that during the pre-industrial period only natural emissions  
 334 occurred without any anthropogenic input. After the industrialization ( $\approx 1750$ ) any increase in  
 335 the emission budget is considered to be due to anthropogenic input while natural emissions  
 336 remain constant, allowing separation of  $E_{\text{nat}}$  and  $E_{\text{anth}}$ .

337 Hence, the isotopic signature of the pre-industrial (natural) N<sub>2</sub>O source calculated this way  
 338 also represents the isotopic signature of the natural source at present, and consequently the  
 339 average isotopic composition of N<sub>2</sub>O originating from “anthropogenic” sources ( $\delta_{\text{anth}}$ ) can be  
 340 estimated.

## 341 **2.6 Uncertainty estimation using random scenarios**

342 The precision of the calculated N<sub>2</sub>O emissions ( $E_{\text{nat}}$ ,  $E_{\text{anth}}$ ) depends primarily on the precision  
 343 of the atmospheric reconstruction of the N<sub>2</sub>O mole fraction ( $\chi_T$ ). However, the uncertainty  
 344 envelope provided by the firm air reconstruction is insufficient to quantify the uncertainty on  
 345 the atmospheric N<sub>2</sub>O reconstruction: the year-to-year variability of N<sub>2</sub>O is constrained by the  
 346 N<sub>2</sub>O lifetime in the troposphere, which is very small in comparison to the width of the  
 347 reconstructions confidence interval. Possible realistic N<sub>2</sub>O scenarios are scenarios that are  
 348 within the confidence intervals provided by the atmospheric reconstructions, and that have  
 349 realistic year-to-year variability.

350 Mathematically, this can be represented by an uncertainty variance covariance matrix **B**,  
 351 where the diagonal elements (variances) are the yearly uncertainties on the atmospheric N<sub>2</sub>O  
 352 mole fractions, and the off-diagonals are the covariances of the uncertainties of different  
 353 years. The covariance between the uncertainty on the reconstruction in one year  $i$  and the  
 354 uncertainty in another year  $j$  is defined as:

$$355 \quad cov(i,j)=r_{i,j}\sigma_i\sigma_j \quad (9)$$

$$356 \quad r_{i,j}=f(|i-j|) \quad (10)$$

357 The correlation ( $r_{i,j}$ ) is maximum between two consecutive years, and decreases as the time  
 358 difference increases.



359 We generated an ensemble of 50 random realistic  $\text{N}_2\text{O}$  scenarios within the uncertainty  
360 envelope of the firm atmospheric  $\text{N}_2\text{O}$  reconstruction constrained by the covariance matrix  $\mathbf{B}$ .  
361 For each of these atmospheric  $\text{N}_2\text{O}$  scenarios, we calculated the corresponding  $\text{N}_2\text{O}$  emission  
362 time series. The range of emissions from these scenarios then provides a realistic estimate for  
363 the uncertainty in  $\text{N}_2\text{O}$  emissions.

364 We carried out the same analysis for the different  $\text{N}_2\text{O}$  isotopocules: for each isotopocule ( $\delta$   
365 value), we generated a covariance matrix  $\mathbf{B}^\delta$ , constrained by the uncertainty ranges provided  
366 by the atmospheric reconstructions and the correlation coefficients defined in Eq.6 and Eq.7  
367 to generate a set of 50 random scenarios within the uncertainty envelopes. For each of these  
368 random scenarios, we calculated the corresponding source signature scenario and the range in  
369 the results provides an uncertainty estimate of the isotopic source signatures.

### 370 **3 Results**

#### 371 **3.1 Mean age**

372 The mean age of  $\text{N}_2\text{O}$  in air sampled from different depths in the firn for all datasets that are  
373 used in this study is shown in Fig. 1. The strong change in the mean age gradient that is  
374 clearly visible in each profile reflects the transition between the diffusive and bubble close-off  
375 zones, which occurs at a specific depth and mean age for each site (marked with x on Fig.1).  
376 Fig. 1 also shows that for each site the few samples that are collected within the bubble close-  
377 off zone provide the constraints for most of the reconstructed record (for instance, at BKN-03,  
378 50 m depth is the beginning of the bubble close-off zone). In addition to the mean age, the  
379 width of the age spectrum also increases with depth. Therefore, the temporal resolution of  
380 signals that can be reconstructed from the firn air measurements reduces with depth and  
381 approaches the one of ice core samples towards the bottom of the bubble close-off zone.

382 The Greenland sites (NH) have similar meteorological and glaciological conditions (Table 1),  
383 thus the differences between the mean age profiles in Fig. 1 are small. The Antarctic sites  
384 (SH) show clear differences because the meteorological and glaciological variables differ  
385 strongly from site to site. As a result the firn-ice transition is at a different depth for each  
386 location (e.g., the firn-ice transition zone for DML-98 is located at about 73.5 m compared to  
387 about 99.5 m at DC-99).



### 3.2 Experimental results and multi-site reconstruction

Mole fraction and isotopic composition of  $\text{N}_2\text{O}$  in firn air are presented versus depth of the firn air sampling in the middle panels of Fig. 2. The mole fraction decreases with depth in qualitative agreement with the known increase of  $\text{N}_2\text{O}$  in the atmosphere over time. In contrast, all isotope deltas slowly increase with depth in the upper firn and show stronger heavy isotope enrichment in the close-off zone, both indicating heavy isotope depletion in atmospheric  $\text{N}_2\text{O}$  with time.

The atmospheric history that has been reconstructed from these firn datasets using the multi-site inversion (using the data from NEEM-09, NEEM-EU-08, NGRIP-01, BKN-03, DC-99, DML-98) as described in section 2.4 is shown in the left panels of Fig. 2. The solid line shows the scenario that leads to the best fit with all firn data in the middle panel, and the dashed lines show the upper and lower range of possible scenarios that would still produce an acceptable fit to the data within the uncertainty bars. Color-coded symbols show data plotted at their respective mean age (as derived from the firn air model). When the best-fit scenario is used as input for the forward firn air model for each individual site, the model produces the vertical profiles that are shown as coloured lines together with the data in the middle panels. For the sites that were included in the multi-site reconstruction, the firn profiles based on the best-fit scenarios generally match the experimental data points well, which is expected after a successful inversion procedure and with consistent data sets. The right panels in Fig. 2 show the differences between these model results and the data. For the data that were used in the multi-site inversion the model-data differences are generally very small, although individual firn drilling sites in some cases show small systematic deviations, in particular in the close-off zone. This means that when inversions would have been performed on individual sites, the optimal reconstructions would be slightly different. The advantage of the multi-site reconstruction is that the reconstructed scenario is constrained by all sites and all sampling depths. Despite the small differences between individual sites, the left panels show that all data fall within the uncertainty bars of the reconstructed scenario of the inversion.

From 1940 to 2008 the total changes of the  $\delta$  values of atmospheric  $\text{N}_2\text{O}$  are  $(-2.2 \pm 0.2) \text{‰}$  for  $\delta^{15}\text{N}^{\text{av}}$ ,  $(-1.0 \pm 0.3) \text{‰}$  for  $\delta^{18}\text{O}$ ,  $(-1.3 \pm 0.6) \text{‰}$  for  $\delta^{15}\text{N}^{\text{a}}$  and  $(-2.8 \pm 0.6) \text{‰}$  for  $\delta^{15}\text{N}^{\text{b}}$  respectively (Fig. 2, left panels). The average linearized trends are  $(-0.032 \pm 0.004) \text{‰ a}^{-1}$  for  $\delta^{15}\text{N}$ ,  $(-0.014 \pm 0.008) \text{‰ a}^{-1}$  for  $\delta^{18}\text{O}$ ,  $(-0.019 \pm 0.015) \text{‰ a}^{-1}$  for  $\delta^{15}\text{N}^{\text{a}}$  and  $(-0.041 \pm 0.020) \text{‰ a}^{-1}$  for  $\delta^{15}\text{N}^{\text{b}}$ . These overall trends are slightly lower compared to previous studies that used



only the data at individual sites (Ishijima et al., 2007; Bernard et al., 2006; Röckmann et al., 2003; Sowers et al., 2002) and other studies that used data from the same period, which were not used in the present study (Park et al., 2012). However, the differences lie well within the combined uncertainties. We note that comparisons of average linear trends can be flawed when the firm air records have different length and the temporal profiles do not change linearly (see below). Trends for  $\delta^{15}\text{N}^{\alpha}$  are smaller in magnitude than for  $\delta^{15}\text{N}^{\beta}$ , while results from Bernard et al. (2006) showed stronger changes for  $\delta^{15}\text{N}^{\alpha}$  than for  $\delta^{15}\text{N}^{\beta}$ . However, in that study the trends were largely determined from measurements on young ice core samples with comparatively higher measurement errors and scatter.

Data from two sites were not included in the multi-site inversion and are used as independent validation of the reconstructed scenarios. The data points from Ishijima et al. (2007) (NGRIP-01, yellow) are within the range of scenarios reconstructed by the inverse model and thus independently validate our results. The  $\delta^{15}\text{N}^{\text{av}}$  and  $\delta^{18}\text{O}$  data from Sowers et al. (2002) (SP-01 in light blue and SP-95 in blue) however, agree only for the more recent atmospheric history (Fig.2, left panels). For mean ages before 1990 most of the points are outside the uncertainty envelopes of the multi-site reconstruction. Inter-laboratory calibration differences might be a possible explanation for the discrepancy, but the differences are not a systematic shift, and they are larger than offsets among laboratories that were established in the past (Sapart et al., 2011; Kaiser et al., 2003). In fact, the data reported by Sowers et al., (2002) were actually measured with good agreement in two different laboratories.

To evaluate our scaling approach we repeated the multi-site reconstruction using the original non re-scaled data and the data that were re-scaled to NEEM-09 instead of DC-99 (see Appendix C). The data rescaled to NEEM-09 gave very similar results (within uncertainties) to the one re-scaled to DC-99 as was expected, thus the results do not depend on the choice of the site used for re-scaling. Without re-scaling, the overall change of  $\text{N}_2\text{O}$  mole fraction and isotopic composition remained the same, but an additional decadal variability was introduced for  $\delta^{15}\text{N}^{\text{av}}$ ,  $\delta^{15}\text{N}^{\alpha}$  and  $\delta^{15}\text{N}^{\beta}$ . In addition to that, the uncertainty envelopes doubled because of the scale inconsistencies. All scaling approaches produce results that are consistent with our preferred scaling to DC-99 within the uncertainty envelopes. We conclude that DC-99 re-scaling removed the discrepancies that would cause larger errors if the original data were used instead, but the re-scaling does not introduce artificial signals (see Appendix C).



451 The regularization of the inversion results using a rugosity factor introduces a free parameter,  
452 which is chosen to eliminate overfitting of experimental uncertainties and which controls the  
453 smoothness of the reconstruction. The value of this parameter is set based on a robust  
454 generalized cross validation criterion, ensuring that the resolution obtained from the inverse  
455 model is similar to the experimental data while taking into account the sparsity of the  
456 measurements (Witrant and Martinerie, 2013). A sensitivity experiment where the weight of  
457 the regularization term is increased, which leads to comparable results as linear tropospheric  
458 histories presented in Fig. 2 was performed (Appendix C). This combined with the fact that  
459 straight lines can be drawn within the uncertainty envelopes of the reconstructed scenarios  
460 and the sensitivity tests (see Appendix C) indicates that the isotopic trends are not  
461 significantly different from straight lines within the current uncertainties.

### 462 3.3 Reconstruction of the N<sub>2</sub>O emission history

463 Fig. 3 shows the temporal evolution of the global N<sub>2</sub>O mole fraction as inferred from the firn  
464 air reconstruction in the top panel, and in the bottom panel the emission strength in Tg a<sup>-1</sup> N  
465 calculated with the mass balance model (Section 2.5). The solid black line denotes the best  
466 estimate scenario, which is used as input in the mass balance model. The magenta lines show  
467 the ensemble of random scenarios generated to quantify the uncertainty of the emissions (see  
468 Section 2.6).

469 The increase in the N<sub>2</sub>O mole fraction of (32±1) nmol mol<sup>-1</sup> over the reconstruction period  
470 can be explained in the mass balance model by an increase in the emissions from (11.9±1.7)  
471 Tg a<sup>-1</sup> N in 1940 to (16.4±1.7) Tg a<sup>-1</sup> N in 2008. The emissions increased with an increasing  
472 trend until 1975, then the annual increase continued, but at a slower rate up to 1990, and from  
473 then on the annual emissions have stayed approximately constant or even decreased slightly.  
474 The corresponding changes in the mole fraction (increasing growth rate before 1990, no  
475 increase and possibly slight decrease in the growth rate afterwards) are difficult to discern due  
476 to the long atmospheric lifetime of N<sub>2</sub>O. On average, the annual growth rate from 1995 to  
477 2008 period is 0.7 nmol mol<sup>-1</sup> a<sup>-1</sup>, corresponding to average annual emissions of 3.5 Tg a<sup>-1</sup> N.

### 478 3.4 The temporal evolution of the N<sub>2</sub>O isotope signatures

479 The results from the isotope budget calculations are presented in Fig. 4. The left panels show  
480 the atmospheric trends. The solid black lines represent the best-fit scenarios while the dashed  
481 black lines represent the upper and lower uncertainty envelope of the firn air reconstructions.





482 The magenta lines represent 50 scenarios generated randomly within the reconstructed  
483 uncertainty range, as described in section 2.6. The middle panels show the temporal changes  
484 in the isotope signatures of the total  $\text{N}_2\text{O}$  source, with their accompanied uncertainties, as  
485 calculated from the atmospheric mass balance model (section 2.5). The total source is split  
486 into an assumed constant "natural" and an increasing "anthropogenic" component and the  
487 right panels show the isotopic evolution of the "anthropogenic" component.

488 Results show that the average  $\delta^{15}\text{N}^{\text{av}}$  of the total  $\text{N}_2\text{O}$  source, over the reconstruction period, is  
489  $(-7.6 \pm 0.6) \text{‰}$  where the uncertainty is calculated using the  $1\sigma$  uncertainty from the scenarios  
490 with respect to the mean value (magenta lines). There is no statistically significant long-term  
491 trend, but a temporal variability is observed on the decadal scale that might mask this trend.  
492  $\delta^{15}\text{N}^{\text{av}}$  first decreased from  $(-6.5 \pm 0.6) \text{‰}$  in 1940 to  $(-8.5 \pm 0.6) \text{‰}$  in 1965, then slowly  
493 increased again to  $(-6.6 \pm 0.6) \text{‰}$  in 1985, followed by another decrease to  $(-8.5 \pm 0.6) \text{‰}$  in  
494 2008. These oscillations originate from the slightly curved trends in the isotopic  
495 reconstructions for  $\delta^{15}\text{N}^{\text{av}}$  in Fig. 5 (left panels).

496 When the source is split into a constant natural and a varying anthropogenic component, the  
497 variability is primarily projected on the anthropogenic part and the temporal variations  
498 increase accordingly. However, also the uncertainties increase substantially, because the  
499 differences between the individual scenarios are attributed to only a small fraction of the total  
500 source.

501 The  $\delta^{15}\text{N}^{\text{av}}$  signature of the anthropogenic source has an average value of  $(-18.2 \pm 2.6) \text{‰}$ . It  
502 initially increases (the small initial decrease is not significant) from  $(-21.5 \pm 2.6) \text{‰}$  in 1940 to  
503  $(-8.6 \pm 2.6) \text{‰}$  in 1990 where it starts to slowly decrease reaching  $(-15.4 \pm 2.6) \text{‰}$  in 2008.  
504 During the early part of the reconstruction period ( $<1970$ ), when the "anthropogenic"  
505 contribution was only a small fraction of the total source, the uncertainty ranges of the source  
506 signatures are large. Therefore, the uncertainties for the early part ( $<1970$ ) were excluded  
507 from the uncertainty  $1\sigma$  uncertainties from the generated scenarios. This applies to all  
508 anthropogenic isotope signatures.

509 The budget calculations suggest an overall trend towards more enriched anthropogenic  
510 emissions but the uncertainties are very large. Mathematically, this trend arises from the fact  
511 that the isotope reconstructions yield relatively linear temporal isotope trends, whereas the  
512 source strength increases in a strongly non-linear fashion (Fig. 4). In the beginning of the  
513 record a small increase in the source strength needs to produce a similar absolute isotope shift



514 as a larger increase in the source strength in later years. This can only be satisfied by a lower  
515  $\delta^{15}\text{N}^{\text{av}}$  value for the small “anthropogenic” emissions in the early part of the firm record. A  
516 constant  $\delta^{15}\text{N}^{\text{av}}$  source signature would result in a small temporal change in  $\delta^{15}\text{N}^{\text{av}}$  of  
517 atmospheric  $\text{N}_2\text{O}$  in the beginning of the record and increasing isotope trends with increasing  
518 emissions, similar to the exponential curves that were fit to the firm air data in Röckmann et  
519 al. (2003).

520 The  $\delta^{18}\text{O}$  of the total source varies within  $(27.2 \pm 2.6) \text{‰}$  over the entire period.  $\delta^{18}\text{O}$  does not  
521 show significant decadal scale oscillations because the reconstructed scenario for  $\delta^{18}\text{O}$  is even  
522 more strictly linear than the  $\delta^{15}\text{N}^{\text{av}}$  scenario. For this reason, as explained above, in the best fit  
523 scenario the  $\delta^{18}\text{O}$  of the anthropogenic source for the initial 30 years has a more depleted  
524 value starting with  $(15.2 \pm 2.6) \text{‰}$  in year 1940, reaching  $(31.1 \pm 2.6) \text{‰}$  in year 1975 and  
525 remaining around this value until 2008 (Fig. 5). However, the relatively larger uncertainty  
526 envelopes for the atmospheric history of  $\delta^{18}\text{O}$  actually allow scenarios with smaller  $\delta^{18}\text{O}$   
527 changes in the beginning of the record and larger changes in the later period, which means  
528 that the reconstruction does not exclude a constant value for the anthropogenic  $\delta^{18}\text{O}$  source  
529 signature. The available dataset thus does not allow quantifying a long-term trend in  $\delta^{18}\text{O}$ .

530 For the position dependent  $^{15}\text{N}$  signatures of the total source no significant long-term trends  
531 were detected. For  $\delta^{15}\text{N}^{\text{a}}$  no decadal scale variability is observed, whereas for  $\delta^{15}\text{N}^{\text{b}}$  a  
532 temporal variability is observed similar to the  $\delta^{15}\text{N}^{\text{av}}$ . The uncertainty ranges for  $\delta^{15}\text{N}^{\text{a}}$  and  
533  $\delta^{15}\text{N}^{\text{b}}$  are about a factor 2 greater than for  $\delta^{15}\text{N}^{\text{av}}$ , which is due to the larger analytical error  
534 that leads to higher uncertainties in the scenario reconstructions.  $\delta^{15}\text{N}^{\text{a}}$  varies in the range  $(-3.0 \pm 1.9) \text{‰}$ ,  $\delta^{15}\text{N}^{\text{b}}$  in the range  $(-11.7 \pm 2.3) \text{‰}$ .

536 The temporal evolution of  $\delta^{15}\text{N}^{\text{a}}$  of the anthropogenic source looks similar to that of  $\delta^{18}\text{O}$ , but  
537 with even larger variations and uncertainties with a total average of  $(-8.1 \pm 1.7) \text{‰}$ .  $\delta^{15}\text{N}^{\text{a}}$   
538 increased from  $(-18.2 \pm 1.7) \text{‰}$  in 1940 to an average of  $(-5.4 \pm 1.7) \text{‰}$  in 1975 and retained  
539 this value until 2008. In contrast,  $\delta^{15}\text{N}^{\text{b}}$  is similar to that of  $\delta^{15}\text{N}^{\text{av}}$  with a total anthropogenic  
540 source average of  $(-26.1 \pm 8.4) \text{‰}$ .  $\delta^{15}\text{N}^{\text{b}}$  initially decreases from  $(-19.1 \pm 8.4) \text{‰}$  to  $(-42.0 \pm 8.4) \text{‰}$   
541 in 1955 only to increase again to  $(-10.6 \pm 8.4) \text{‰}$  in year 1990 and then decrease again to  $(-26.0 \pm 8.4) \text{‰}$   
542 in 2008.



#### 543 **4 Discussion**

544 From the combination of the firm air reconstruction with a simple two-box model we conclude  
545 that  $\text{N}_2\text{O}$  emissions increased from  $(11.9 \pm 1.7) \text{ Tg a}^{-1} \text{ N}$  in 1940 to  $(16.4 \pm 1.7) \text{ Tg a}^{-1} \text{ N}$  in  
546 2008. This agrees, within uncertainties, with previous firm reconstruction studies from  
547 Ishijima et al. (2007) and Park et al. (2012) and bottom-up approaches using emission  
548 databases (Syakila and Kroeze, 2013; Kroeze et al., 1999). A more recent study by Thompson  
549 et al. (2014b) performed inversions of atmospheric measurements for 2006 to 2008 with  
550 multiple models and reported emissions of  $16.1\text{--}18.7 \text{ Tg a}^{-1} \text{ N}$  for 2008 in agreement with our  
551 findings.

552 To investigate the effect of lifetime choice on the  $\text{N}_2\text{O}$  isotopic signatures (Prather et al.  
553 (2015) we performed a sensitivity study where we linearly changed the  $\text{N}_2\text{O}$  lifetime from 123  
554 years pre-industrially ( $\approx 1750$ ) to 119 years in modern times (2008). The results are shown in  
555 Appendix D, where the effect on the emission strength and isotopic composition is discussed  
556 in detail. Results from this sensitivity study showed that the effect of a decreasing lifetime  
557 gives higher  $\text{N}_2\text{O}$  emissions for year 2008 while keeping the same pre-industrial value,  
558 confirming a sensitivity in the choice of lifetime in line with Prather et al. (2015).  
559 Consequently this sensitivity only influences the anthropogenic isotopic signature by 10 %,  
560 meaning that the resulting values can increase by  $(2.0 \pm 1.0) \%$ . The lifetime effect is most  
561 pronounced for the earliest part of the record ( $< 1970$ ) where the reconstruction uncertainties  
562 are larger than this systematic uncertainty.

563 The increase in  $\text{N}_2\text{O}$  emissions over the past decades resulted in an overall decrease of all  
564 isotopic signatures of atmospheric  $\text{N}_2\text{O}$  with time. The isotopic signature of the total source of  
565  $\text{N}_2\text{O}$  (Fig. 4, middle panels) is strongly depleted in all heavy isotopes compared to  
566 tropospheric  $\text{N}_2\text{O}$  (Table 3), which is due to the strong enrichment associated with the  
567 removal in the stratosphere. In Table 3 the isotopic composition for the pre-industrial period  
568 ( $\approx 1750$ ) ( $\delta_{\text{nat,pi}}$ ) is compared with the derived anthropogenic source signature derived from  
569 our multi-site reconstruction ( $\delta_{\text{anth}}$ , averaged from 1940 to 2008). The results show that the  
570 anthropogenic source is more depleted in heavy isotopes than the natural one for all  
571 signatures, confirming results from previous studies that used forward firm air modelling on  
572 measurements from individual sites (Park et al., 2012; Ishijima et al., 2007; Röckmann et al.,  
573 2003).



574 Anthropogenic N<sub>2</sub>O emissions are dominated by agricultural soil (70 %) with smaller  
575 contributions from automobiles, coal combustion, biomass burning and industry. Oceanic  
576 emissions were previously assumed to be only natural. However, the latest IPCC Assessment  
577 Report (IPCC, ch.6, 2013) for the first time breaks down oceanic emissions into a natural and  
578 an anthropogenic component, e.g. due to atmospheric N deposition to rivers (Syakila and  
579 Kroeze, 2011; Duce et al., 2008; Kroeze et al., 2005), thus estimating the anthropogenic  
580 component of oceanic N<sub>2</sub>O emissions to amount to 1 Tg a<sup>-1</sup> N.

581 N<sub>2</sub>O emitted from agricultural soils and biomass burning is more depleted in  $\delta^{15}\text{N}$  and  $\delta^{18}\text{O}$   
582 than the tropospheric background (Park et al., 2011; Goldberg et al., 2010; Ostrom et al.,  
583 2010; Tilsner et al., 2003; Perez et al., 2001; 2000) while N<sub>2</sub>O emitted from other minor  
584 sources, such as automobiles, coal combustion and industry, has values closer to tropospheric  
585 N<sub>2</sub>O values (Syakila and Kroeze, 2011; Toyoda et al., 2008; Ogawa and Yoshida, 2005a;  
586 2005b).

587 Qualitatively, an increase of strongly depleted agricultural emissions in the first part of our  
588 reconstruction, followed by a decreasing relative contribution from agriculture and increasing  
589 contributions from more enriched sources like industry, automobiles and coal combustion,  
590 can explain the reconstructed changes of isotope signatures of both the total source and the  
591 anthropogenic component. The global N<sub>2</sub>O budget study from Syakila and Kroeze (2011)  
592 indicates that agricultural emissions were 78 % of the total during the 1940-1980 period with  
593 little input from industry, vehicle exhaust and coal combustion. After 1980 the relative share  
594 of agricultural emissions dropped to 64 %, while the other sources increased, supporting our  
595 suggestion.

596 Additional evidence for potential changes in the N<sub>2</sub>O source composition between the pre-  
597 industrial and present atmosphere may be derived from the position-dependent  $^{15}\text{N}$  signatures,  
598 quantified by the  $^{15}\text{N}$  site preference. Table 3 shows that the difference in the  $\delta^{15}\text{N}^{\text{av}}$  signature  
599 between the pre-industrial and the anthropogenic source derived from our reconstruction is  
600 primarily due to a change at position  $\delta^{15}\text{N}^{\beta}$ , whereas  $\delta^{15}\text{N}^{\alpha}$  remains relatively constant. This is  
601 reflected by a larger difference in  $\delta^{15}\text{N}^{\text{sp}}$  between natural and anthropogenic emissions, which  
602 could indicate a temporal change in production processes.

603 Sutka et al. (2006) suggested that there may be two distinct classes of N<sub>2</sub>O sources with  
604 different  $\delta^{15}\text{N}^{\text{sp}}$ . N<sub>2</sub>O produced during nitrification and fungal denitrification had a high  $\delta^{15}\text{N}^{\text{sp}}$   
605 of (33±5) ‰ and N<sub>2</sub>O from denitrification and nitrifier denitrification had a low  $\delta^{15}\text{N}^{\text{sp}}$  of



606 (0±5) ‰. Park et al., (2012) used these two endmembers to calculate a change in the relative  
 607 fractions of these source classes over time based on their firm air data. Although this approach  
 608 is strongly simplified and several other sources and factors may contribute (Toyoda et al.,  
 609 2015), we use the results from our box model calculations (Table 3) in a similar way to  
 610 estimate the fraction of the two source categories according to the following simple mass  
 611 balance calculation:

$$612 \quad F_{\text{high}} = \frac{\delta^{15}\text{N}_{\text{meas}}^{\text{sp}} - \delta^{15}\text{N}_{\text{low}}^{\text{sp}}}{\delta^{15}\text{N}_{\text{high}}^{\text{sp}} - \delta^{15}\text{N}_{\text{low}}^{\text{sp}}} \quad (11)$$

613 This returns a fractional contribution of the  $\delta^{15}\text{N}_{\text{high}}^{\text{sp}}$  component of (19±4) % to the total pre-  
 614 industrial emissions and (35±11) % to the total present source. The errors were derived by  
 615 propagating the errors of the  $\delta^{15}\text{N}^{\text{sp}}$  endmembers and  $\delta^{15}\text{N}_{\text{meas}}^{\text{sp}}$  as given above. We note that  
 616 the errors associated with the precise isotopic composition of the endmembers are correlated  
 617 if  $\delta^{15}\text{N}^{\text{sp}}$  for the two endmembers remain relatively constant. Therefore, the change in the  
 618 relative fraction of the two categories is likely better constrained than the absolute values.

619 Splitting the total present emission strength into a natural (pre-industrial, 11.0 Tg a<sup>-1</sup> N) and  
 620 anthropogenic (5.4 Tg a<sup>-1</sup> N) component, we derive a fraction of the  $\delta^{15}\text{N}_{\text{high}}^{\text{sp}}$  component  
 621 (which includes nitrification) of (54±26) % for the "anthropogenic" emissions. This is another  
 622 piece of evidence for agricultural sources being the main contributor to the N<sub>2</sub>O increase,  
 623 because nitrification-dominated agricultural emissions can be associated with the  $\delta^{15}\text{N}_{\text{high}}^{\text{sp}}$   
 624 component.

625 The temporal changes of the derived fraction of nitrification are in good qualitative agreement  
 626 with the results from Park et al. (2012), who reported a change of (13±5) % from 1750 to  
 627 (23±13) % today. However, the absolute numbers derived from our study are higher than the  
 628 results from Park et al. (2012). The difference is due to the fact that different apparent isotope  
 629 fractionations during stratospheric removal ( $\epsilon_{\text{app}}$ ) are used in the mass balance model (Table  
 630 3; eq. 7,8). In this study we used the averaged lowermost stratospheric apparent isotope  
 631 fractionations from Kaiser et al. (2006), which we consider more representative than the  
 632 numbers used by Park et al. (2012). Using different values for  $\epsilon_{\text{app}}$  causes a shift in the  
 633 isotopic source signatures from the mass balance model. The choice of this value thus adds a  
 634 systematic source of uncertainty to the absolute value of the  $\delta^{15}\text{N}_{\text{high}}^{\text{sp}}$  fractions reported above  
 635 ( $F_{\text{high}}$ ).



636 Nevertheless, this systematic uncertainty should not alter the overall *change* in  $F_{\text{high}}$  from pre-  
637 industrial to modern times and the results from our multi-site reconstruction of the isotopic  
638 composition of  $\text{N}_2\text{O}$  thus confirm the suggestion by Park et al. (2012) that the relative  
639 importance of the high-SP component (presumably nitrification) has increased with increasing  
640 mole fraction since pre-industrial times.

## 641 5 Conclusions

642 The temporal evolution of the total  $\text{N}_2\text{O}$  emission fluxes and the source isotopic composition  
643 have been estimated in a top-down approach using a multi-site reconstruction of  $\text{N}_2\text{O}$  mole  
644 fraction and isotopic composition from 6 firm air samplings at 5 different Arctic and Antarctic  
645 locations in a two-box model. The results from a mass balance model constraints the source  
646 strength and suggest a total increase in  $\text{N}_2\text{O}$  emissions of  $(4.5 \pm 1.7) \text{ Tg a}^{-1} \text{ N}$  between the 1940  
647 and 2008 due to anthropogenic processes. This agrees with previous top-down estimates, but  
648 deviates from bottom-up model estimates, which suggest higher  $\text{N}_2\text{O}$  emission increases. A  
649 significant source of the uncertainty in such top-down estimates is a possible change in the  
650  $\text{N}_2\text{O}$  lifetime over the reconstruction period, which we have quantified following the recent  
651 results from Prather et al. (2015).

652 The reconstruction of mole fraction and isotopic composition was used to investigate  
653 temporal changes in the isotopic signature of  $\text{N}_2\text{O}$  emissions over the study period. The  
654 average total source for  $\delta^{15}\text{N}^{\text{av}}$  and  $\delta^{15}\text{N}^{\beta}$  shows no statistically significant long-term trend but  
655 likely significant decadal scale variability. For  $\delta^{18}\text{O}$  and  $\delta^{15}\text{N}^{\alpha}$  of the total  $\text{N}_2\text{O}$  source, no  
656 significant temporal changes can be detected with the present dataset because the  
657 uncertainties are large, especially in the beginning of the reconstruction period.

658 When the total source is split into a constant natural and a varying anthropogenic component,  
659 the reconstruction of the  $\delta$  values of the anthropogenic source indicates a significant increase  
660 of  $\delta^{15}\text{N}^{\text{av}}$  from the early to the modern part of the record. This originates from the near-linear  
661 isotope histories of the best guess scenario, which would imply that small emissions in the  
662 early part had a similar absolute effect on the  $\delta$  values as stronger emissions in the latter part.  
663 A similar effect for  $\delta^{18}\text{O}$  is likely, but not significant given the larger uncertainties for this  
664 signature.

665 Nevertheless, the isotope signal in  $\delta^{15}\text{N}^{\text{av}}$  may also be a signal for changing source  
666 contributions over time. Bottom-up models suggest that  $\text{N}_2\text{O}$  emitted from agricultural soils



667 was the dominant contributor to the anthropogenic N<sub>2</sub>O increase in the first decades. Smaller  
668 contributions due to emissions from more enriched sources, like industry, automobiles and  
669 coal combustion increased, which may have contributed to an isotope enrichment of the  
670 emissions, which is not detectable within the error bars for the other isotope signatures.

671 Results from the mass balance model yield an increase in <sup>15</sup>N site preference between the pre-  
672 industrial and modern total N<sub>2</sub>O source. The increase in  $\delta^{15}\text{N}^{\text{sp}}$  of (16±11) % between the pre-  
673 industrial and modern source is in qualitative agreement with increased emissions from  
674 nitrification processes associated with agriculture.

### 675 **Acknowledgements**

676 We thank the teams involved in the firm air sampling at NEEM site during the 2008 and 2009  
677 field seasons. NEEM is directed and organized by the Centre of Ice and Climate at the Niels  
678 Bohr Institute, University of Copenhagen, Denmark and the US National Science Foundation,  
679 Office of Polar Programs. It is supported by funding agencies and institutions in Belgium  
680 (FNRS-CFB and FWO), Canada (NRCan/GSC), China (CAS), Denmark (FIST), France  
681 (IPEV, CNRS/INSU, CEA and ANR), Germany (AWI), Iceland (RannIs), Japan (NIPR),  
682 Korera (KOPRI), The Netherlands (NWO/ALW and NWO/NPP), the United Kingdom  
683 (NERC NE/F021194/1) and the USA (US NSF, Office of Polar Programs). This project was  
684 financially supported by the Dutch Science Foundation (NWO), projects 851.30.020 &  
685 865.07.001.



## 686 References

- 687 Allin, S. J., Laube, J. C., Witrant, E., Kaiser, J., McKenna, E., Dennis, P., Mulvaney, R.,  
688 Capron, E., Martinerie, P., Röckmann, T., Blunier, T., Schwander, J., Fraser, P. J.,  
689 Langenferls, R. L., and Sturges, W. T.: Chlorine isotope composition in chlorofluorocarbons  
690 CFC-11, CFC-12 and CFC-113 in firm, stratospheric and tropospheric air, Atmos. Chem.  
691 Phys., 15, 6867-6877, doi:10.5194/acp-15-6867-2015, 2015.
- 692 Bernard, S., Röckmann, T., Kaiser, J., Barnola, J.-M., Fischer, H., Blunier, T., and  
693 Chappellaz, J.: Constraints on N<sub>2</sub>O budget changes since pre-industrial time from new firm air  
694 and ice core isotope measurements, Atmos. Chem. Phys., 6,, 493–503, doi:10.5194/acp-6-  
695 493-2006, 2006.
- 696 Buizert, C., Sowers, T., and Blunier, T.: Assessment of diffusive isotopic fractionation in  
697 polar firm, and application to ice core trace gas records, Earth Planet. Sci. Lett., 361, 110–119,  
698 2013.
- 699 Butterbach-Bahl, K., and Dannenmann, M.: Denitrification and associated soil N<sub>2</sub>O emissions  
700 due to agricultural activities in a changing climate, Curr. Op. Environ. Sus., 3(5), 389–395,  
701 doi:10.1016/j.cosust.2011.08.004, 2011.
- 702 Ciais, P., Sabine, C., Bala, G., Bopp, L., Brovkin, V., Canadell, J., Chhabra, A., DeFries, R.,  
703 Galloway, J., Heimann, M., Jones, C., Le Quéré, C., Myneni, R.B., Piao, S., and Thornton, P.:  
704 Carbon and other biogeochemical cycles. Climate Change 2013: The Physical Science Basis,  
705 Contribution of Working Group I to the Fifth Assessment Report of the Intergovernmental  
706 Panel on Climate Change, Cambridge University Press, Cambridge, United Kingdom and  
707 New York, NY, USA, 2013.
- 708 Crutzen, P. J., Mosier, A. R., Smith, K. A., and Winiwarter, W.: N<sub>2</sub>O release from agro-  
709 biofuel production negates global warming reduction by replacing fossil fuels, Atmos. Chem.  
710 Phys., 8, 389-395, doi:10.5194/acp-8-389-2008, 2008.,
- 711 Davidson, E. A.: The contribution of manure and fertilizer nitrogen to atmospheric nitrous  
712 oxide since 1860, Nat. Geosci., 2(9), 659–662, doi:10.1038/ngeo608, 2009.





- 713 Duce, R. A., LaRoche, J., Altieri, K., Arrigo, K. R., Baker, A. R., Capone, D. G., Cornell, S.,  
714 Dentener, F., Galloway, J., and Ganeshram, R. S.: Impacts of atmospheric anthropogenic  
715 nitrogen on the open ocean, *Science*, 320, 893-897, 2008.
- 716 Freing, A., Wallace, D. W. R., and Bange, H. W.: Global oceanic production of nitrous oxide,  
717 *Phil. Trans. R. Soc. Lond., Series B*, 367(1593), 1245–55, doi:10.1098/rstb.2011.0360, 2012.
- 718 Hirsch, A., Michalak, A., Bruhwiler, L., Peters, W., Dlugokencky, E., and Tans, P.: Inverse  
719 modelling estimates of the global nitrous oxide surface flux from 1998-2001, *Gl. Biochem.*  
720 *Cycl.*, 20, GB 1008, doi: 10.1029/2004GB002443, 2006.
- 721 Holton, J. R.: On the global exchange of mass between stratosphere and troposphere, *J.*  
722 *Atmos. Sci.*, 47(3), 392-395, 1990.
- 723 Houghton, J. T., Meira Filho, L. G., Bruce, J., Lee, H., Callander, B. A., Haites, E., Harris, N.,  
724 and Maskell, K.: *Climate Change 1994: Radiative Forcing of Climate Change and an*  
725 *Evaluation of the IPCC IS 92 Emission Scenarios*, Cambridge University Press, Cambridge,  
726 UK, 1994.
- 727 Ishijima, K., Sugawara, S., Kawamura, K., Hashida, G., Morimoto, S., Murayama, S., Aoki,  
728 S.: Temporal variations of the atmospheric nitrous oxide concentration and its  $\delta^{15}\text{N}$  and  $\delta^{18}\text{O}$   
729 for the latter half of the 20th century reconstructed from firn air analyses, *J. Geophys. Res.*,  
730 112(D3), doi:10.1029/2006JD007208, 2007.
- 731 Kaiser, J., Brenninkmeijer, C.A.M., Röckmann, T.: Intramolecular  $^{15}\text{N}$  and  $^{18}\text{O}$  fractionation  
732 in the reaction of  $\text{N}_2\text{O}$  with  $\text{O}(^1\text{D})$  and its implications for the stratospheric  $\text{N}_2\text{O}$  isotopic  
733 signature, *J. Geophys. Res.*, 107 (4214), doi:10.1029/2001JD001506, 2002.
- 734 Kaiser, J., Röckmann T., and Brenninkmeijer, C.A.M.: Complete and accurate mass  
735 spectrometric isotope analysis of tropospheric nitrous oxide, *J. Geophys. Res.*, 108(D15), 1–  
736 17, doi:10.1029/2003JD003613, 2003.
- 737 Kaiser, J., Engel, A., Borchers, R., and Röckmann, T.: Probing stratospheric transport and  
738 chemistry with new balloon and aircraft observations of the meridional and vertical  $\text{N}_2\text{O}$   
739 isotope distribution, *Atmos. Chem. Phys.*, 6, 3535-3556, doi:10.5194/acp-6-3535-2006, 2006.



- 740 Kaiser, J., and Röckmann T.: Correction of mass spectrometric isotope ratio measurements  
741 for isobaric isotopologues of O<sub>2</sub>, CO, CO<sub>2</sub>, N<sub>2</sub>O and SO<sub>2</sub>, *Rap. Commun. Mass Spec.*, 3997–  
742 4008, doi: 10.1002/rcm.3812, 2008.
- 743 Kim, K. R., and Craig, H.: Nitrogen-15 and Oxygen-18 Characteristics of Nitrous Oxide: A  
744 global perspective, *Science*, 262, 1855-1857, 1993.
- 745 Kim, K. R., Craig, H.: Two-isotope characterization of N<sub>2</sub>O in the Pacific Ocean and  
746 constraints on its origin in deep water, *Nature*, 347, 58-61, doi:10.1038/347058a0, 1990.
- 747 Kool, D. M., Wrage, N., Oenema, O., Harris, D., and Groenigen, J. W. Van.: The <sup>18</sup>O  
748 signature of biogenic nitrous oxide is determined by O exchange with water, *Rap. Commun.*  
749 *Mass Spec.*, 104–108, doi:10.1002/rcm.3859, 2009.
- 750 Kroeze, C., Mosier, A., and Bouwman, L.: Closing the global N<sub>2</sub>O budget: a retrospective  
751 analysis 1500-1994, *Glob. Biogeochem. Cycl.*, 13, 1-8, doi: 10.1029/1998GB900020, 1999.
- 752 Kroeze, C., Dumont, E., and Seitzinger, S. P.: New estimates of global emissions of N<sub>2</sub>O from  
753 rivers and estuaries, *Environ. Science*, 2, 159-165, doi:10.1080/15693430500384671, 2005.
- 754 Löschner, C.R., Kock, A., Könneke, M., LaRoche, J., Bange, H. W., and Schmitz, R. A.:  
755 Production of oceanic nitrous oxide by ammonia-oxidizing archaea, *Biogeosciences*, 9, 2419–  
756 2429, doi:10.5194/bg-9-2419-2012, 2012.
- 757 Maeda, K., Toyoda, S., Shimojima, R., Osada, T., Hanajima, D., Morioka, R., and Yoshida,  
758 N.: Source of nitrous oxide emissions during the cow manure composting process as revealed  
759 by isotopomer analysis of and amoA abundance in betaproteobacterial ammonia-oxidizing  
760 bacteria, *Appl. Environ. Microbiol.*, 76(5), 1555–62, doi:10.1128/AEM.01394-09, 2010.
- 761 Martinerie, P., Nourtier-Mazauric, E., Barnola, J.-M., Sturges, W. T., Worton, D. R., Atlas,  
762 E., Brasseur, G. P.: Long-lived halocarbon trends and budgets from atmospheric chemistry  
763 modelling constrained with measurements in polar firn, *Atmos. Chem. Phys.*, 9, 3911-3934,  
764 doi:10.5194/acp-9-3911-2009, 2009.



- 765 McLinden, C. A., Prather, M. J., Johnson M. S.: Global modeling of the isotopic analogues of  
766 N<sub>2</sub>O: Stratospheric distributions, budgets and the <sup>17</sup>O-<sup>18</sup>O mass-independent anomaly, J.  
767 Geophys. Res., 108(D8), doi:10.1029/2002JD002560, 2003.
- 768 Minschwaner, K., Salawitch, R.J., McElroy, M.B.: Absorption of Solar Radiation by O<sub>2</sub>:  
769 Implications for O<sub>3</sub> and lifetimes of N<sub>2</sub>O, CFC<sub>13</sub>, and CF<sub>2</sub>Cl<sub>2</sub>, J. Geophys. Res., 98, 10543-  
770 10561, doi: 10.1029/93JD00223, 1993.
- 771 Ogawa, M., and Yoshida, N.: Intramolecular distribution of stable nitrogen and oxygen  
772 isotopes of nitrous oxide emitted during coal combustion, Chemosphere, 61, 877-887, 2005a.
- 773 Ogawa, M., and Yoshida, N.: Nitrous oxide emission from the burning of agricultural residue.  
774 Atmos. Environ., 39, 3421-3429, 2005b.
- 775 Ostrom, N. E., and Ostrom, P. H.: The isotopomers of Nitrous Oxide: Analytical  
776 considerations and application to resolution of microbial production pathways, Baskaran, M.,  
777 Handbook of Environmental Isotope Geochemistry, Advances in Isotope Geochemistry,  
778 Springer, Verlag, Berlin, Heidelberg, 453-476, 2011.
- 779 Park, S., Atlas, E. L., and Boering, K. A.: Measurements of N<sub>2</sub>O isotopologues in the  
780 stratosphere: Influence of transport on the apparent enrichment factors and the isotopologue  
781 fluxed to the troposphere, J. Geophys. Res., 109, doi:10.1029/2003JD003731, 2004.
- 782 Park, S., Croteau, P., Boering, K. A., Etheridge, D. M., Ferretti, D., Fraser, P. J., and  
783 Trudinger, C. M.: Trends and seasonal cycles in the isotopic composition of nitrous oxide  
784 since 1940, Nat. Geosci., 5(4), 261-265, doi:10.1038/ngeo1421, 2012.
- 785 Pérez, T., Trumbore, S. E., Tyler, S. C., Davidson, E. A., Keller, M., and Camargo, P. de.:  
786 Isotopic variability of N<sub>2</sub>O emissions from tropical forest soils, Glob. Biogeochem. Cycl.,  
787 14(2), 525-535, 2000.
- 788 Pérez, T., Trumbore, S. E., Tyler, S. C., Matson, P. A., Ortiz-Monasterio, I., Rahn, T., and  
789 Griffith, D. W. T.: Identifying the agricultural imprint on the global N<sub>2</sub>O budget using stable  
790 isotopes, J. Geophys. Res., 106(D9), 9869-9878, 2001.



- 791 Popp, B. N., Westley, M. B., Toyoda, S., Miwa, T., Dore, J. E., Yoshida, N., Rust, T. M.,  
792 Sansone, F. J., Russ, M. E., Ostrom, N. E., and Ostrom, P. H: Nitrogen and oxygen  
793 isotopomeric constraints on the origins and sea-to-air flux of N<sub>2</sub>O in the oligotrophic  
794 subtropical North Pacific gyre, Glob. Biogeochem. Cycl., 16, 1064,  
795 doi:10.1029/2001GB001806, 2002.
- 796 Potter, K. E.: Nitrous oxide (N<sub>2</sub>O) isotopic composition in the troposphere: instrumentation,  
797 observations at Mace Head, Ireland, and regional modeling, PhD thesis, Department of Earth,  
798 Atmospheric, and Planetary Sciences at the Massachusetts Institute of Technology, 2011.
- 799 Prather, M. J., et al.: Measuring and modeling the lifetime of nitrous oxide including its  
800 variability, J. Geophys. Res. Atmos., 120, 5693-5705, doi: 10.1002/2015JD023267, 2015.
- 801 Ravishankara, A. R., Daniel, J. S., and Portmann, R. W.: Nitrous oxide (N<sub>2</sub>O): the dominant  
802 ozone-depleting substance emitted in the 21<sup>st</sup> century, Science, 326(5949), 123–125,  
803 doi:10.1126/science.1176985, 2009.
- 804 Röckmann, T., Kaiser, J., Brenninkmeijer, C. A. M., Crowley, J. N., Borchers, R., Brand, W.  
805 A., and Crutzen, J.: Isotopic enrichment of nitrous oxide (<sup>15</sup>N<sup>14</sup>NO, <sup>14</sup>N<sup>15</sup>NO, <sup>14</sup>N<sup>14</sup>N<sup>18</sup>O) in  
806 the stratosphere and in the laboratory, J. Geophys. Res., 106(D10), 10403-10410,  
807 doi:10.1029/2000JD900822, 2001.
- 808 Röckmann, T., Kaiser, J., Brenninkmeijer, C. A. M., and Brand, W. A.: Gas  
809 chromatography/isotope-ratio mass spectrometry method for high-precision position-  
810 dependent <sup>15</sup>N and <sup>18</sup>O measurements of atmospheric nitrous oxide, Rap. Commun. Mass  
811 Spectrom., 17(16), 1897–1908, doi:10.1002/rcm.1132, 2003.
- 812 Röckmann, T., Kaiser, J., Brenninkmeijer, C. A. M.: The isotopic fingerprint of the pre-  
813 industrial and the anthropogenic N<sub>2</sub>O source, Atmos. Chem. Phys., 3, 315-323,  
814 doi:10.5194/acp-3-315-2003, 2003.
- 815 Röckmann, T., and Levin, I.: High-precision determination of the changing isotopic  
816 composition of atmospheric N<sub>2</sub>O from 1990 to 2002, J. Geophys. Res., 110(D21), 1–8,  
817 doi:10.1029/2005JD006066, 2005.



- 818 Santoro, A. E., Buchwald, C., Mellvin, M. R., and Casciotti, K. L.: Isotopic signature of N<sub>2</sub>O  
819 produced by marine ammonia-oxidizing archaea, *Science*, 333(6047), 1282–1285,  
820 doi:10.1126/science.1208239, 2011.
- 821 Sapart, C. J., van der Veen, C., Vigano, I., Brass, M., van de Wal, R. S. W., Bock, M.,  
822 Fischer, H., Sowers, T., Buizert, C., Sperlich, P., Blunier, T., Behrens, M., Schmitt, J., Seth,  
823 B., and Röckmann, T.: Simultaneous stable isotope analysis of methane and nitrous oxide of  
824 ice core samples, *Atmos. Meas. Tech.*, 4, 2607–2618, doi:10.5194/amt-4-2607-2011, 2011.
- 825 Sapart, C. J., Martinerie, P., Witrant, E., Chappellaz, J., van de Wal, R. S. W., Sperlich, P.,  
826 van der Veen, C., Bernard, S., Sturges, W. T., Blunier, T., Schwander, J., Etheridge, D.,  
827 Röckmann, T.: Can the carbon isotopic composition of methane be reconstructed from multi-  
828 site firn air measurements?, *Atmos. Chem. Phys.*, 13, 6993–7005, doi:10.5194/acp-13-6993-  
829 2013, 2013.
- 830 Stocker, T. F., Qin, D., Plattner, G.-K., Tingor, M., Allen, S. K., Boschung, J., Nauels, A.,  
831 Xia, Y., Bex, V., Midgley, P. M. et al.: IPCC, 2013: Climate Change 2013: The physical  
832 Science Basis. Contribution of Working Group I to the Fifth Assessment Report of the  
833 Intergovernmental Panel on Climate Change, Cambridge University Press, Cambridge, United  
834 Kingdom and New York, NY, USA, 2013.
- 835 Sowers, T., Rodebaugh, A., Yoshida, N., and Toyoda, S.: Extending records of the isotopic  
836 composition of atmospheric N<sub>2</sub>O back to 1800 A.D. from air trapped in snow at the South  
837 Pole and the Greenland Ice Sheet Project II ice core, *Global Biogeochemical Cycles*, 16(4),  
838 1–10, doi: 10.1029/2002GB001911, 2002.
- 839 SPARC, 2013: SPARC Report on the Lifetimes of Stratospheric Ozone-Depleting  
840 Substances, Their Replacements, and Related Species, edited by: Ko, M., Newman, P.,  
841 Reimann, S., and Strahan, S, SPARC Report No. 6, WCRP-15, Zurich, Switzerland, 2013.
- 842 Suntharalingam, P., Buitenhuis, E., Le Quéré, C., Dentener, F., Nevison, C., Butler, J. H., and  
843 Forster, G.: Quantifying the impact of anthropogenic nitrogen deposition on oceanic nitrous  
844 oxide, *Geophysical Research Letters*, 39, doi:10.1029/2011GL050778, 2012.
- 845 Sutka, R. L., Ostrom, N. E., Ostrom, P. H., Breznak, J. A., Gandhi, H., Pitt, A. J., and Li, F.:  
846 Distinguishing Nitrous Oxide Production from Nitrification and Denitrification on the Basis



- 847 of Isotopomer Abundances, Appl. Environ. Microbiol., 72(1), 638–644,  
 848 doi:10.1128/AEM.72.1.638-644.2006, 2006.
- 849 Syakila, A., Kroeze, C., and Slomp, C. P.: Neglecting sinks for N<sub>2</sub>O at the earth's surface:  
 850 does it matter?, Journal of Integrative Environmental Sciences, 7, 79–87,  
 851 doi:10.1080/1943815X.2010.497492, 2010.
- 852 Syakila, A., and Kroeze, C.: The global nitrous oxide budget revisited, Greenhouse Gas  
 853 Measurement and Management, 1(1), 17–26, doi:10.3763/ghgmm.2010.0007, 2011.
- 854 Thompson, R. L., Ishijima, K., Saikawa, E., Corazza, M., Karstens, U., Patra, P. K.,  
 855 Bousquet, P. (2014). TransCom N<sub>2</sub>O model inter-comparison, Part II: Atmospheric inversion  
 856 estimates of N<sub>2</sub>O emissions. *Atmospheric Chemistry and Physics Discussions*, 14(4), 5271–  
 857 5321.
- 858 Thompson, R. L., Patra, P. K., Ishijima, K., Saikawa, E., Corazza, M., Karstens, U.,  
 859 Bousquet, P.: TransCom N<sub>2</sub>O model inter-comparison – Part 1: Assessing the influence of  
 860 transport and surface fluxes on tropospheric N<sub>2</sub>O variability, Atmos. Chem. Phys. 14, 4349–  
 861 4368, doi:10.5194/acp-14-4349-2014, 2014.
- 862 Toyoda, S., Yamamoto, S., Arai, S., Nara, H., Yoshida, N., Kashiwajura, K., and Akiyama,  
 863 K.: Isotopomeric characterization of N<sub>2</sub>O produced, consumed and, emitted by automobiles.,  
 864 Rap. Comm. in Mass Spec., 22, 603–612, doi:10.1002/rcm.3400, 2008.
- 865 Witrant, E., Martinerie, P., Hogan, C., Laube, J.C., Kawamura, K., Capron, E., Montzka, S.  
 866 A., Dlugokencky, E. J., Etheridge, D., Blunier, T., and Sturges, W. T.: A new multi-gas  
 867 constrained model of trace gas non-homogeneous transport in firn: evaluation and behavior at  
 868 eleven polar sites, Atmos. Chem. Phys., 12, 11465–11483, doi:10.5194/acp-12-11465-2012,  
 869 2012.
- 870 Witrant, E., Martinerie, P.: Input estimation from sparse measurements in LPV systems and  
 871 isotopic ratios in polar firn, IFAC Joint conference SSSC - 5th Symposium on System  
 872 Structure and Control, Grenoble, France, 150, 2013.



873 Westley, M. B., Popp, B. N., and Rust, T. M.: The calibration of the intramolecular isotope  
874 distribution in nitrous oxide measured by isotope ratio mass spectrometry, Rap. Comm. in  
875 Mass. Spec., 21(3), 391-405, doi:10.1002/rcm.2828, 2007.

876 Yoshida, N., and Toyoda, S.: Constraining the atmospheric N<sub>2</sub>O budget from intramolecular  
877 site preference in N<sub>2</sub>O isotopomers, Nature, 405, 330–334, doi:10.1038/35012558, 2000.

878

879

880



881 Table 1. Site information on the drilling locations of the North Greenland Ice core Project  
 882 (NGRIP-01), Berkner Island (BKN-03), North Greenland Eemian Ice drilling Project  
 883 (NEEM-EU-08, NEEM-09), Dome Concordia (DC-99) and Dronning Maud Land (DML-98),  
 884 where firn air samples were collected, and two key meteorological variables of each site.

Site	Location	Mean annual temperature (°C)	Surface accumulation rate (water equivalent) (cm a <sup>-1</sup> )	Sampling year
NGRIP-01	75° N 42° W	-31	20	2001
BKN-03	79° S 45° W	-26	13	2003
NEEM- EU-08	77.4° N 51.1° W	-29	22	2008
NEEM-09	77.4° N 51.1° W	-29	22	2009
DC-99	75° S 123° E	-53	3	1999
DML-98	75° S 65° E	-38	6	1998

885

886 Table 2. Detailed information in the mole fraction and the isotopic composition of the  
 887 laboratory reference gases used for correcting each set of firn air samples.

Site	Sampling year	Mole fraction (nmol mol <sup>-1</sup> )	$\delta^{15}\text{N}^{\text{av}}$ (‰)	$\delta^{18}\text{O}$ (‰)	$\delta^{15}\text{N}^{\beta}$ (‰)	$\delta^{15}\text{N}^{\alpha}$ (‰)
NGRIP-01	2001	318	6.64	44.61	-2.79	16.07
BKN-03	2003	318	6.64	44.61	-2.79	16.07
NEEM- EU-08	2008	324	6.22	44.40	-3.08	15.52
NEEM-09	2009	318	6.38	44.92	-2.66	15.41
DC-99	1999	318	6.64	44.61	-2.79	16.07
DML-98	1998	318	6.64	44.61	-2.79	16.07

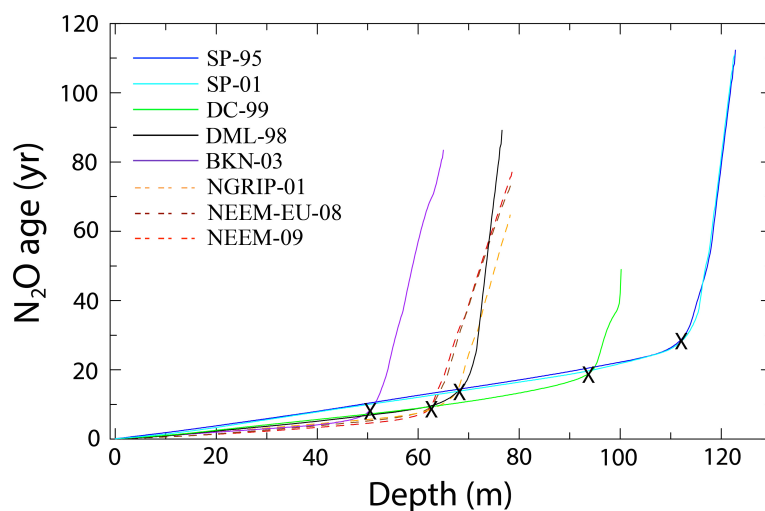




Table 3. Stratospheric isotope fractionation ( $\epsilon_{\text{app}}$ ) used in the mass balance model, and isotopic composition of the natural and anthropogenic source, and the respective results from Park et al. (2012).

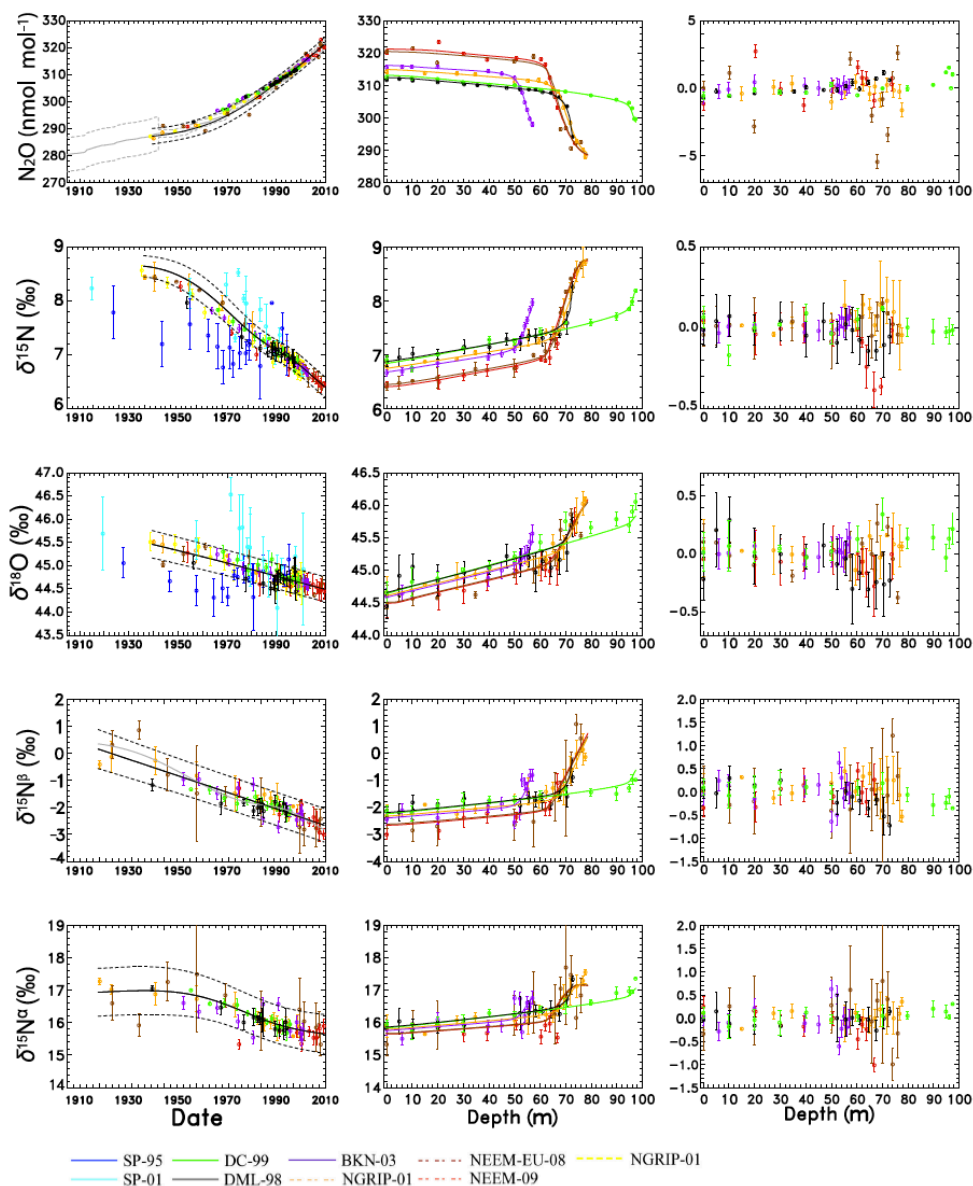
	$\epsilon_{\text{app}}$ (‰)	$\epsilon_{\text{app}}$ (‰)	$\delta_{\text{atm,pi}}$ (‰)	$\delta_{\text{nat,pi}}$ (‰)	$\delta_{\text{nat,pi}}$ (‰)	$\delta_{\text{anth}}$ (‰)	$\delta_{\text{anth}}$ (‰)
	this study*	Park et al., 2012*	Park et al., 2012	this study*	Park et al., 2012	this study*	Park et al., 2012**
$\delta^{15}\text{N}$	-16.2	-14.9	$9.3 \pm 0.2$	$-5.2 \pm 0.2$	$-5.3 \pm 0.2$	$-18.2 \pm 2.6$	$-15.6 \pm 1.2$
$\delta^{18}\text{O}$	-13.4	-13.3	$45.5 \pm 0.2$	$33.1 \pm 0.2$	$32.0 \pm 0.2$	$27.2 \pm 2.6$	$32.0 \pm 1.3$
$\delta^{15}\text{N}^{\alpha}$	-23.0	-22.4	$18.8 \pm 1.0$	$-1.9 \pm 1.0$	$-3.3 \pm 1.0$	$-8.1 \pm 1.7$	$-7.6 \pm 6.2$
$\delta^{15}\text{N}^{\beta}$	-9.4	-7.1	$-0.6 \pm 1.1$	$-8.3 \pm 1.1$	$-7.5 \pm 1.1$	$-26.1 \pm 8.4$	$-20.5 \pm 7.1$
$\delta^{15}\text{N}^{\text{sp}}$	-	-	$19.4 \pm 1.5$	$6.4 \pm 1.5$	$4.2 \pm 1.5$	$18.0 \pm 8.6$	$13.1 \pm 9.4$

\* $\epsilon_{\text{app}}$  values used in this study are averaged values from the lower stratosphere from Kaiser et al. (2006) and  $\epsilon_{\text{app}}$  values from Park et al. (2012) were used from Park et al. (2004).  $\delta_{\text{atm,pi}}$  values are from Park et al. (2012) who also calculated  $\delta_{\text{nat,pi}}$  and  $\delta_{\text{anth}}$  in a two-box model. Here, the  $\delta_{\text{anth}}$  values are the averaged values over the whole investigated period.



901

902 Figure 1.  $N_2O$  mean ages in firm versus depth. The dashed lines represent the sites from the  
 903 NH (North Greenland Ice-core Project [NGRIP-01], North Eemian Ice-core Project [NEEM-  
 904 09, NEEM-EU-08]) and the solid lines the SH sites (South Pole [SP-01, SP-95], Dome C  
 905 [DC-99], Dolomite [DML-98] and Berkner Island [BKN-03]). The numbers accompanying  
 906 the sites are the corresponding drilling years. Marker X indicates the transition between the  
 907 firm diffusive zone and the bubble close-off zone for each site. Dashed orange line NGRIP-01,  
 908 dashed brown NEEM-EU-08, dashed red NEEM-09, purple line BKN-03, black DML-98,  
 909 green DC-99, blue SP-95 and light blue SP-01.



910

911

912

913



Figure 2. Left: Reconstructed atmospheric scenarios (black solid line with dashed lines indicating the  $2\sigma$  uncertainty intervals) and results of the firm air samples (corrected for firm fractionation) plotted at their respective assigned mean age. Middle: corresponding depth profiles, symbols show the measurements and solid lines the results of the forward model using the best estimate scenario as input. Right: model data discrepancies. Orange: NGRIP-01 (Bernard et al, 2006), Yellow: NGRIP-01 (Ishijima et al., 2007), Brown: NEEM-EU-08, Red: NEEM-09, Purple: BKN-03, Black: DML-98, Green: DC-99, Blue: SP-95 and Light Blue: SP-01. Data from NGRIP-01 (Ishijima et al., 2007), SP-95 and SP-01 were not used in the atmospheric reconstruction and are only plotted for comparison purposes here.

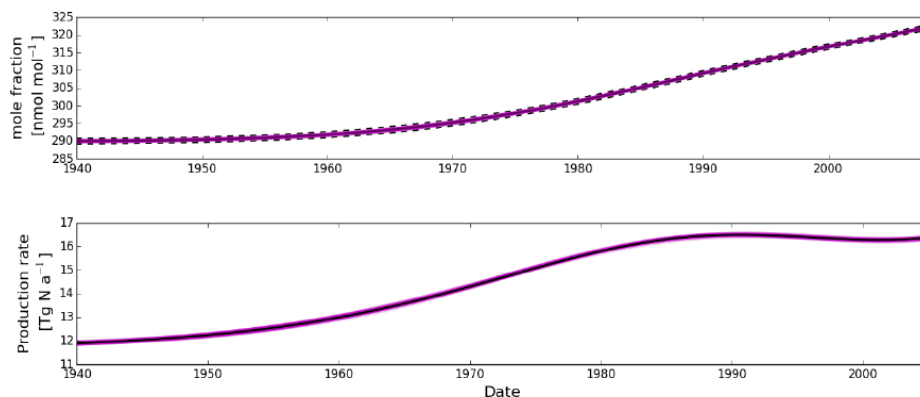
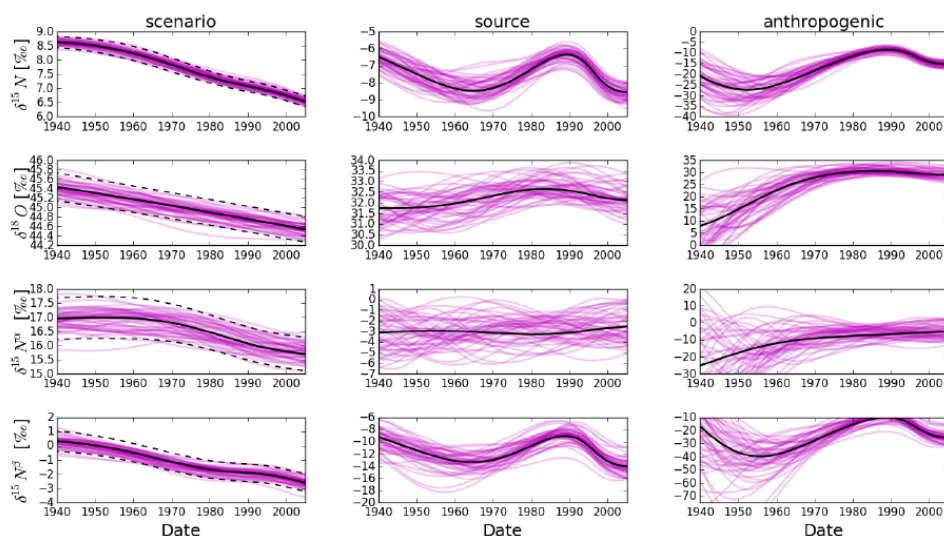


Figure 3: Top panel.  $\text{N}_2\text{O}$  mole fraction history from the multisite reconstruction (solid black line with uncertainty envelopes as dashed black lines) and the scenarios within the uncertainty envelopes that were used in the mass balance model (magenta lines) to evaluate the uncertainties of the atmospheric modelling results. Bottom panel.  $\text{N}_2\text{O}$  production rate as calculated from the mass balance model. The solid black line represents the result for the best fit reconstruction while magenta lines represent the results for the individual scenarios from the top panel.



933

934 Figure 4: Left panels: Historic evolution of  $\delta^{15}\text{N}$ ,  $\delta^{18}\text{O}$ ,  $\delta^{15}\text{N}^{\alpha}$  and  $\delta^{15}\text{N}^{\beta}$  in  $\text{N}_2\text{O}$  as derived  
 935 from the firm air reconstruction. Middle panels: isotope signatures of the total emitted  $\text{N}_2\text{O}$ .  
 936 Middle panels: isotope signatures of the anthropogenic source, respectively. The solid black  
 937 line represents the best-fit scenario while the dashed ones represent the respective  
 938 uncertainties as determined by the reconstruction method. Magenta lines represent the  
 939 emissions that are required to produce the magenta  $\text{N}_2\text{O}$  histories in the left panels.

940

941

942

943

944

945

946

947

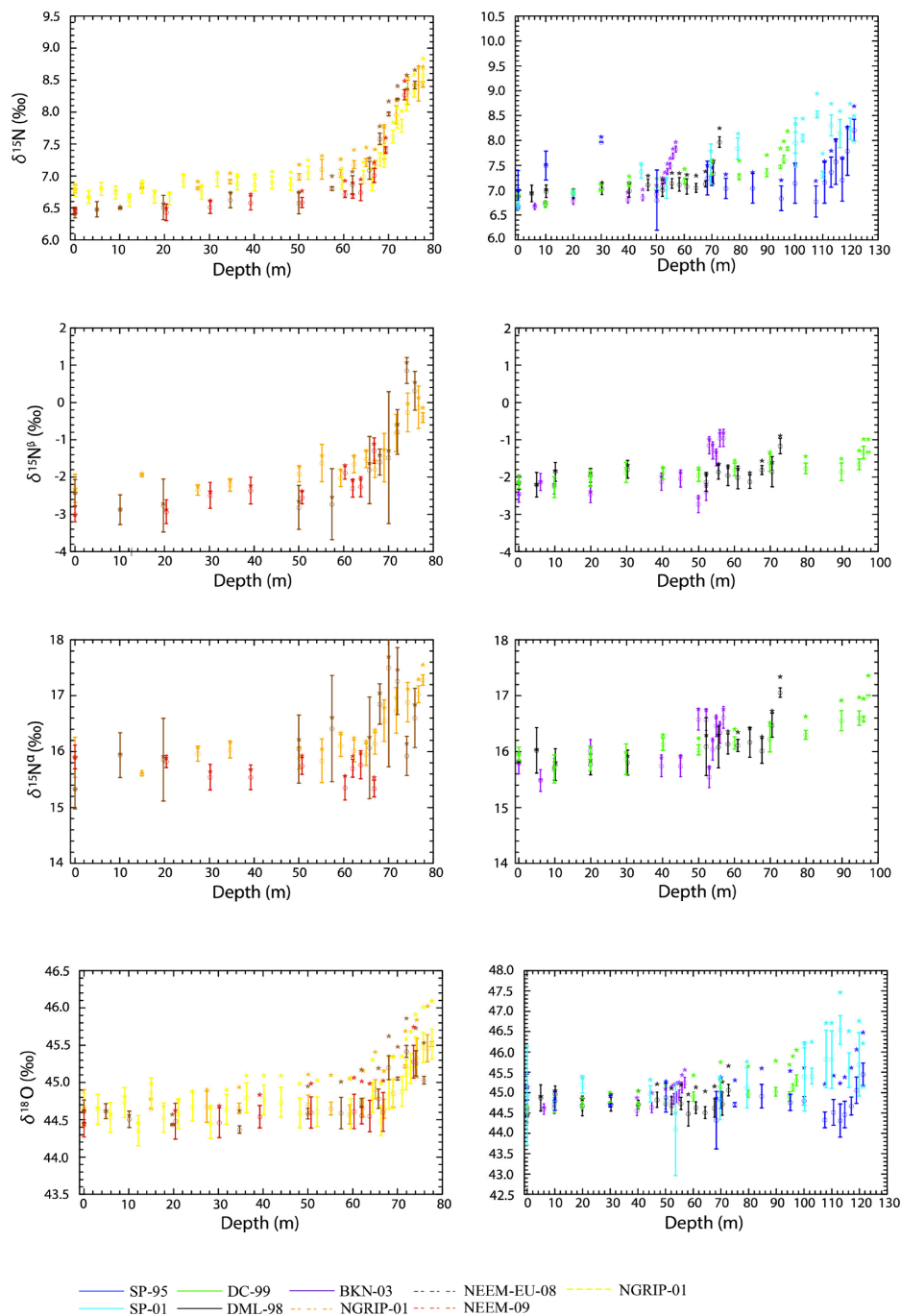
948

949

950



## 951 Appendix A: Effect of firn fractionation on isotopic composition



952



953 Figure A1: Effect of firn fractionation on  $N_2O$  isotopic composition in firn. Original  
954 measurements are plotted as stars, data corrected for firn fractionation are plotted as circles  
955 with error bars. The right hand side shows Southern hemisphere sites, orange: NGRIP-01  
956 (Bernard et al, 2006), yellow: NGRIP-01 (Ishijima et al, 2007), brown: NEEM-EU-08, red  
957 NEEM-09 and the left hand side shows Northern hemisphere sites, purple: BKN-03, black  
958 DML-98, green DC-99, blue SP-95 and light blue SP-01

959

960

961

962

963

964

965

966

967

968

969

970

971

972

973

974

975

976

977

978

979



## 980 **Appendix B: Data processing**

981 In this study isotope deltas ( $\delta$ ) are used to denote the relative  $^{15}\text{N}/^{14}\text{N}$  and  $^{18}\text{O}/^{16}\text{O}$  ratio  
 982 difference of  $\text{N}_2\text{O}$  in firm air with respect to a standard reference,

$$983 \quad \delta^{15}\text{N} = \frac{R_{\text{sample}}}{R_{\text{standard}}} - 1 \quad (1)$$

984 where R represents the  $^{15}\text{N}/^{14}\text{N}$  or  $^{18}\text{O}/^{16}\text{O}$  abundance ratio of a standard or a sample.  $\delta^{15}\text{N}$   
 985 values are reported relative to  $^{15}\text{R}$  of atmospheric  $\text{N}_2$ ,  $\delta^{18}\text{O}$  values relative to  $^{18}\text{R}$  of Vienna  
 986 Mean Standard Ocean Water (VSMOW). The  $^{15}\text{N}/^{14}\text{N}$ ,  $^{18}\text{O}/^{16}\text{O}$  and position dependent  
 987  $^{15}\text{N}/^{14}\text{N}$  isotope ratios were derived from measurement of the  $m/z$  45 /  $m/z$  44,  $m/z$  46 /  $m/z$  44  
 988 and  $m/z$  31 /  $m/z$  30 ion current ratios according to Kaiser et al., (2008), assuming a constant  
 989  $^{17}\text{O}$  excess of 0.9 ‰.

990 There is a disagreement between reported trends of the position dependent  $\delta^{15}\text{N}^{\text{av}}$  values  
 991 reported in the literature from firm air on the one hand and archived air samples on the other  
 992 hand (Park et al., 2012; Ishijima et al., 2007; Bernard et al., 2006; Röckmann and Levin,  
 993 2005; Röckmann et al., 2003; Sowers et al., 2002). In principle the temporal trend measured  
 994 directly on archived air samples should be fully consistent with top firm air samples of the  
 995 various data sets, which were collected over a decade or more, since the air in the diffusive  
 996 zone is not very old. However, this is not the case. Using the high-precision determination of  
 997 the temporal trend of the  $\text{N}_2\text{O}$  isotope signatures on archived air samples from Röckmann and  
 998 Levin (2005) as reported in section 2.4 we rescale the different firm profiles to match this  
 999 trend in the diffusive zone by interpolating the measurements from the diffusive zone of all  
 1000 sites to DC-99 ( $\delta_{\text{INT}}$ ). By using the firm model – assigned mean age of each sample, The  
 1001 maximum age difference from diffusive zone to surface corresponds to  $\Delta\text{age} = \Delta_{\text{DC } t-t_0} = 10$  a.  
 1002 Below you can find the equations used:

$$1003 \quad \delta_{\text{INT}} = \delta_{t-t_0} - \delta_{\text{DC } t-t_0} + m (\Delta_{t-t_0} - \Delta_{\text{DC } t-t_0}) \quad (2)$$

$$1004 \quad \delta_{\text{Final}} = \delta_{\text{meas}} - (\delta_{\text{exp}} - \delta_{\text{INT}}) \quad (3)$$

1005 Where  $m$  is the slope connecting the two points we want to interpolate. The applied scaling  
 1006 ( $\delta_{\text{Final}}$ ) is given in the Table B1 below. To bring the data to the most recent international scale,  
 1007 NOAA-2006A, we used an equation extracted from a correlation between a scale ratio of  
 1008 NOAA-2006A to CSIRO versus the mole fraction of  $\text{N}_2\text{O}$ . The correlation showed higher





1009 scale ratio for low fraction values and lower scale ratio for higher mole fraction values. The  
1010 equation extracted is given below:

1011  $y(\text{NOAA-2006}) = -1.535 \times 10^{-4} y^2(\text{CSIRO}) + 1.045 y(\text{CSIRO})$  (4)



Table B1. Implemented scaling for N<sub>2</sub>O mole fraction and isotopic composition. The re-scaled average was extracted from the diffusivity zone for each site, which corresponds to the top 50 m. The expected trends are averaged values from CSIRO (<http://www.csiro.au/greenhouse-gases>) for the last 30 years for the mole fraction and measured trends from Röckmann and Levin (2005) for the isotopic composition. The rather large corrections to the isotope data from the SP-01 and SP-95 drillings are likely due to inter-laboratory scale differences.

Site	$\gamma(\text{N}_2\text{O})(\text{nmol mol}^{-1})$		
	Re-scaled average	Expected trend change	Correction
DML-98	0.09±0.29	-0.80±0.06	-0.89±0.32
NGRIP-01(Bernard)	3.39±0.54	1.60±0.06	-1.79±0.54
NGRIP-01 (Ishijima)	4.12±0.32	1.60±0.06	-2.52±0.32
BKN-03	3.47±0.22	3.20±0.06	-0.27±0.23
NEEM-EU-08	3.57±1.81	7.20±0.06	3.63±1.81
NEEM-09	8.84±1.82	8.00±0.06	-0.84±1.82

Site	$\delta^{15}\text{N}(\text{‰})$		
	Re-scale average	Expected trend change	Correction
SP-95	1.43±0.56	0.16±0.00	-1.27±0.56
DML-98	-0.18±0.12	0.04±0.00	0.22±0.12
SP-01	0.22±0.22	-0.08±0.00	-0.30±0.22
NGRIP -01(Bernard)	-0.18±0.07	-0.08±0.00	0.10±0.07
NGRIP -01 (Ishijima)	0.17±0.13	-0.08±0.00	-0.25±0.13
BKN-03	-0.17±0.12	-0.16±0.00	0.01±0.12
NEEM-EU-08	-0.63±0.15	-0.36±0.00	0.27±0.15
NEEM-09	-0.43±0.05	-0.40±0.00	-0.03±0.05



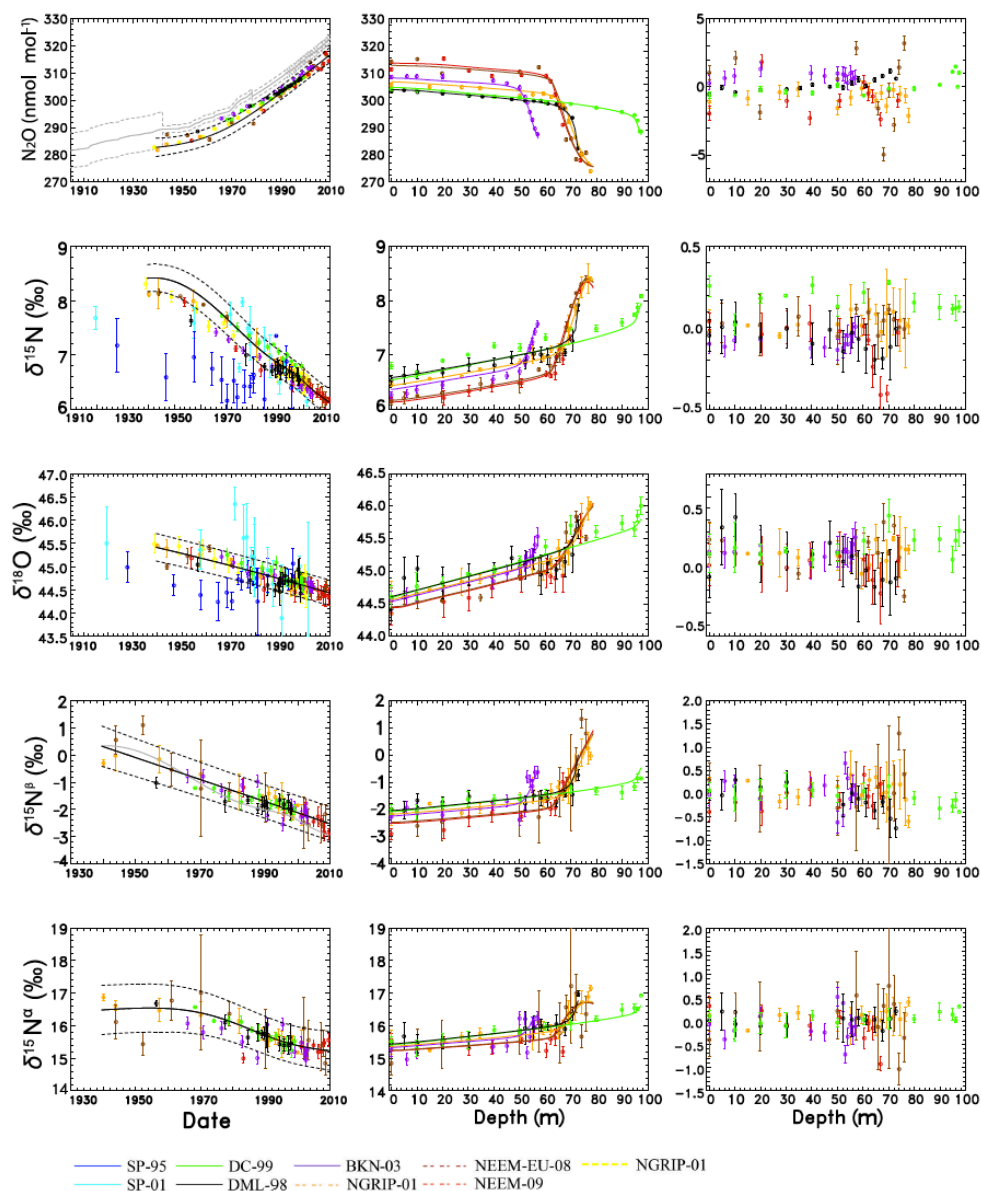
Site	$\delta^{18}\text{O}$ (‰)		
	Re-scale average	Expected trend change	Correction
SP-95	-0.88±0.27	0.08±0.00	0.96±0.27
DML-98	0.26±0.15	0.02±0.00	-0.24±0.15
SP -01	0.74±0.62	-0.04±0.00	-0.78±0.62
NGRIP-01 (Bernard)	-0.08±0.05	-0.04±0.00	0.04±0.05
NGRIP-01 (Ishijima)	-0.17±0.12	-0.04±0.00	0.13±0.12
BKN-03	0.02±0.06	-0.08±0.00	-0.10±0.06
NEEM-EU-08	-0.21±0.15	-0.19±0.00	0.02±0.15
NEEM-09	0.28±0.04	-0.21±0.00	-0.49±0.04

Site	$\delta^{15}\text{N}^{\beta}$ (‰)		
	Re-scale average	Expected trend change	Correction
DML-98	-0.41±0.20	0.06±0.02	0.47±0.20
NGRIP-01 (Bernard)	-0.10±0.25	-0.13±0.02	-0.02±0.25
BKN-03	-0.53±0.30	-0.26±0.02	0.27±0.30
NEEM-EU-08	-0.33±0.27	-0.58±0.02	-0.25±0.27
NEEM-09	-0.14±0.17	-0.64±0.02	-0.50±0.17

Site	$\delta^{15}\text{N}^{\alpha}$ (‰)		
	Re-scale average	Expected trend change	Correction
DML-98	0.09±0.11	0.01±0.02	-0.08±0.11
NGRIP-01 (Bernard)	-0.26±0.19	-0.03±0.02	0.23±0.19
BKN-03	0.19±0.32	-0.06±0.02	-0.25±0.32
NEEM-EU-08	-0.61±0.35	-0.13±0.02	0.48±0.35
NEEM-09	-0.72±0.16	-0.14±0.02	0.58±0.16



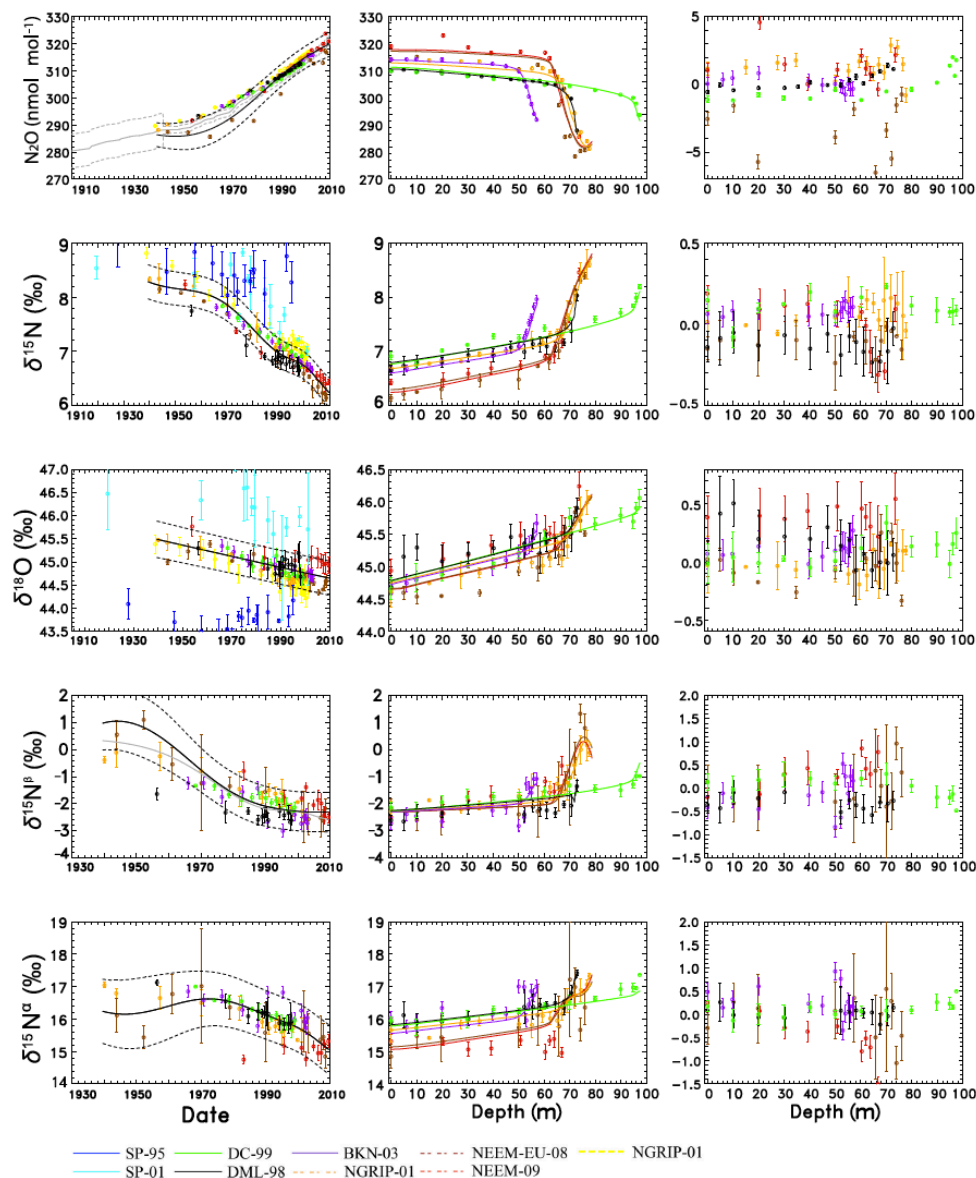
1019 **Appendix C: Atmospheric reconstruction re-scaled to NEEM-09 and without**  
 1020 **data re-scaling**



1021  
 1022 Figure C1. Results of the firn data evaluation (similar to Figure 2) using the data without re-  
 1023 scaling as indicated in the text, Orange: NGRIP-01 (Bernard et al, 2006), Yellow: NGRIP-01

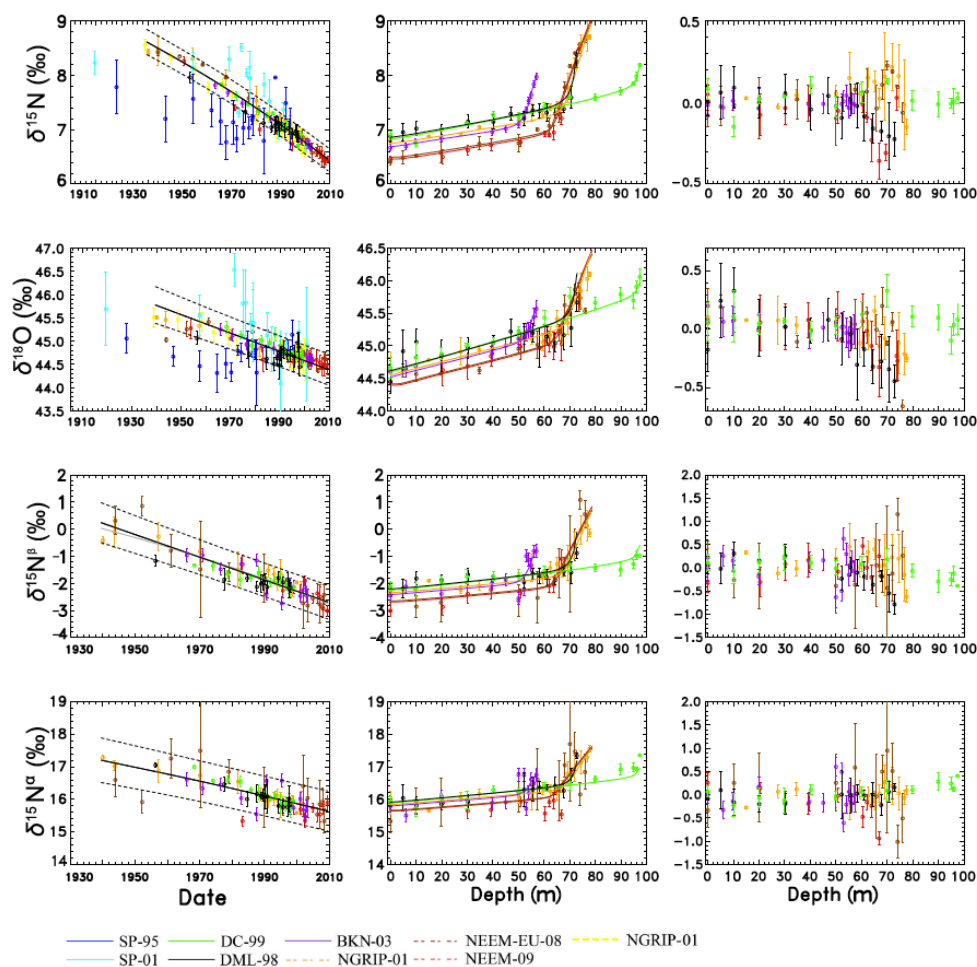


1024 (Ishijima et al, 2007), Brown: NEEM-EU-08, Red: NEEM-09, Purple: BKN-03, Black: DML-  
 1025 98, Green: DC-99, Blue: SP-95 and Light Blue: SP-01.



1026  
 1027 Figure C2. Results of the firn data evaluation (similar to Figure 2) using the data re-scaled to  
 1028 the NEEM-09 site. Colours as in Fig. C1.

1029



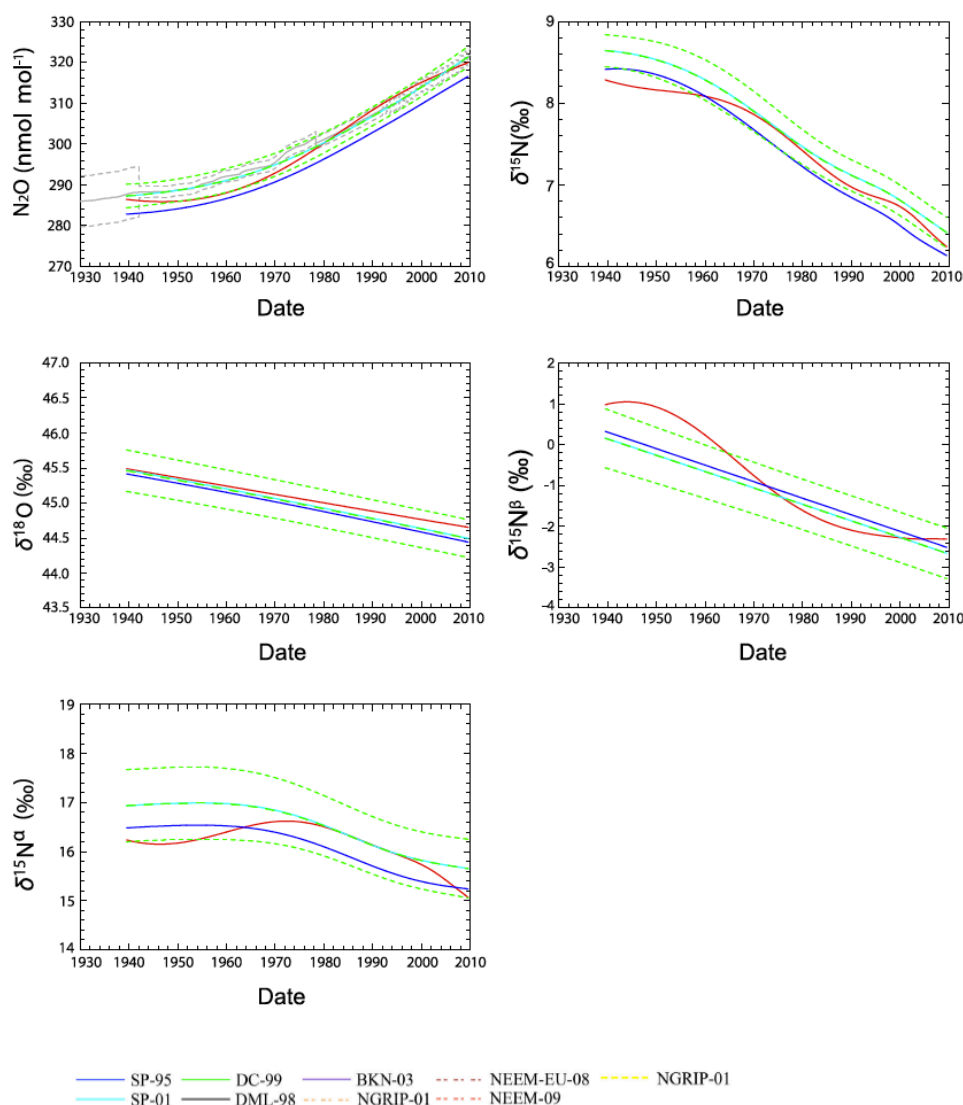
1030

1031 Figure C3. Sensitivity test for the regularization term. Reconstructed atmospheric scenarios  
 1032 (left), corresponding fit of the firm data (centre) and model data discrepancies (right). The best  
 1033 reconstructed scenarios are shown as the black continuous lines, with model derived  
 1034 uncertainties (2σ) in dashed lines. Colours as in Fig. C1.

1035

1036

1037



1038

1039 Figure C4. Comparison of the atmospheric reconstructions between different re-scaling  
 1040 methods. Solid and dashed green lines are the scenarios from data re-scaled to DC-99 used in  
 1041 this study. Solid red lines are the best-case scenario for the non re-scaled data and solid blue  
 1042 lines are the best-case scenarios from the data re-scaled to NEEM-09. The latter data series is  
 1043 shifted because of a calibration offset. When this is corrected for the data superimposes the  
 1044 green lines as expected.

1045



1046 **Appendix D: Sensitivity of the reconstructed N<sub>2</sub>O emissions and isotopic**  
1047 **signatures on N<sub>2</sub>O lifetime.**

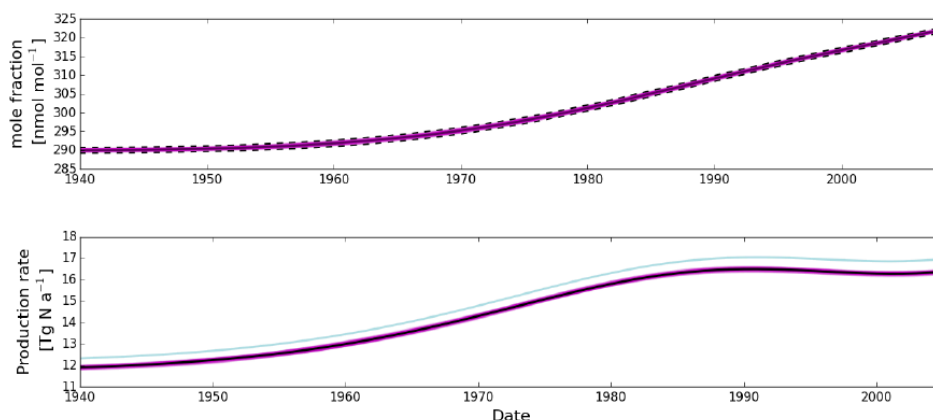
1048 For the default calculations with the mass balance model a constant lifetime for N<sub>2</sub>O was  
1049 used. A recent study from Prather et al. (2015), though, highlighted that top-down model  
1050 calculations are sensitive to changes in the N<sub>2</sub>O lifetime. To quantify the effect on our results  
1051 we performed a sensitivity test where we linearly changed the N<sub>2</sub>O lifetime from pre-  
1052 industrial to modern times from 123 a in 1700 to 119 a in 2008. The results are shown in  
1053 Figures D1 and D2 below.

1054 In Figure D1 the N<sub>2</sub>O atmospheric budget is re-calculated and compared with the results when  
1055 the constant lifetime of  $123^{+29}_{-19}$  a is used. In year 1940 the N<sub>2</sub>O emissions are  $(12.3 \pm 2.7)$  Tg a<sup>-1</sup>  
1056 N and  $(17.0 \pm 1.7)$  Tg a<sup>-1</sup> N in year 2008 with a total increase of  $(4.7 \pm 1.7)$  Tg a<sup>-1</sup> N. When  
1057 keeping the lifetime constant, the results for the same years are  $(11.9 \pm 1.7)$  Tg a<sup>-1</sup> N and  
1058  $(16.4 \pm 1.7)$  Tg a<sup>-1</sup> N with a total increase of  $(4.5 \pm 1.7)$  Tg a<sup>-1</sup> N. This shows that there is a  
1059 sensitivity on the choice of lifetime for our mass balance model on the N<sub>2</sub>O atmospheric  
1060 budget as was indicated by Prather et al. (2015).

1061 The N<sub>2</sub>O source isotopic signature shows no significant change with the choice of lifetime  
1062 giving similar average source values for all source signatures as for when using a constant  
1063 lifetime of  $123^{+29}_{-19}$  a.

1064 On the other hand, the N<sub>2</sub>O average anthropogenic source signature displays a sensitivity in  
1065 the choice of lifetime returning values  $(-15.9 \pm 2.6)$  ‰,  $(28.5 \pm 2.6)$  ‰,  $(-7.2 \pm 1.7)$  ‰ and  $(-22.8 \pm 8.4)$  ‰ for  $\delta^{15}\text{N}^{\text{av}}$ ,  $\delta^{18}\text{O}$ ,  $\delta^{15}\text{N}^{\text{a}}$  and  $\delta^{15}\text{N}^{\text{b}}$  respectively. This agrees within combined  
1066 errors with the total average values of  $(-18.2 \pm 2.6)$  ‰,  $(27.2 \pm 2.6)$  ‰,  $(-8.1 \pm 1.7)$  ‰ and  $(-26.1 \pm 8.4)$  ‰ for  $\delta^{15}\text{N}^{\text{av}}$ ,  $\delta^{18}\text{O}$ ,  $\delta^{15}\text{N}^{\text{a}}$  and  $\delta^{15}\text{N}^{\text{b}}$  respectively when a constant  $123^{+29}_{-19}$  a lifetime  
1067 is used. On average, the N<sub>2</sub>O anthropogenic signature results can differ by 10 % when a  
1068 different lifetime is chosen, which is equivalent to a  $(2.0 \pm 1.0)$  ‰ difference in the final  
1069 anthropogenic values.  
1070  
1071





1072

1073 Figure D1: Top panel. N<sub>2</sub>O mole fraction history from the multisite reconstruction (solid  
 1074 black line with uncertainty envelopes as dashed black lines) and the scenarios within the  
 1075 uncertainty envelopes that were used in the mass balance model (magenta lines) to evaluate  
 1076 the uncertainties of the atmospheric modelling results.

1077 Bottom panel. N<sub>2</sub>O production rate as calculated from the mass balance model assuming a  
 1078 change in the lifetime from 123 a in 1700 to 119 a in 2008 (relative change similar to Prather  
 1079 et al., 2015) in light blue. The solid black line represents the result for the best fit  
 1080 reconstruction while magenta lines represent the results for the individual scenarios from the  
 1081 top panel (lifetime kept constant at 123<sup>+29</sup><sub>-19</sub> a) as used in the main paper.

1082

1083

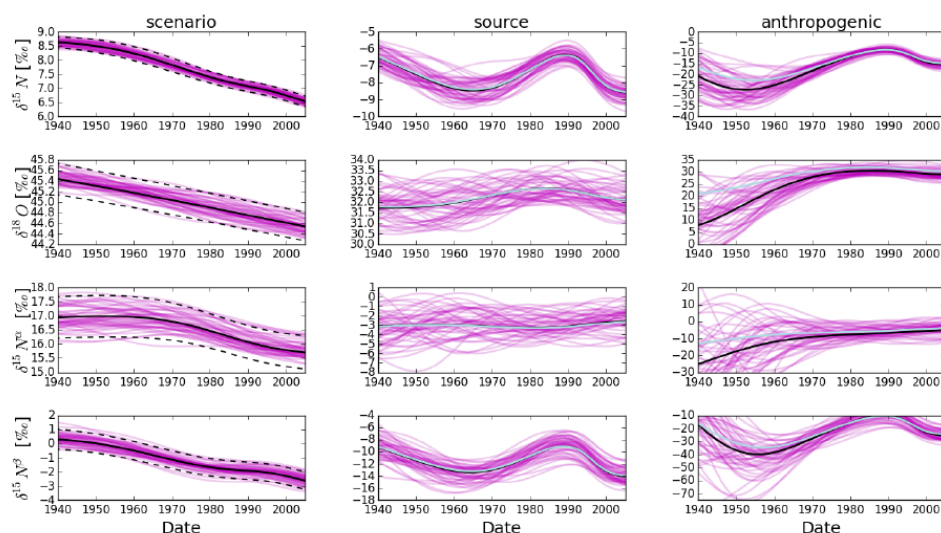
1084

1085

1086

1087

1088



1089

1090 Figure D2: Left panels: Historic evolution of  $\delta^{15}\text{N}$ ,  $\delta^{18}\text{O}$ ,  $\delta^{15}\text{N}^{\alpha}$  and  $\delta^{15}\text{N}^{\beta}$  in  $\text{N}_2\text{O}$  as derived  
 1091 from the firm air reconstruction. The solid black line represents the best-fit scenario while the  
 1092 dashed ones represent the respective uncertainties as determined by the reconstruction  
 1093 method. Magenta lines represent the emissions that are required to produce the magenta  $\text{N}_2\text{O}$   
 1094 histories in the left panels. Middle and right panels: Isotope signatures of the total emitted  
 1095  $\text{N}_2\text{O}$  and anthropogenic source respectively assuming a change in the lifetime from 123 a in  
 1096 1700 to 119 a in 2008 (relative change similar to Prather et al., 2015) in light blue. The solid  
 1097 black line represents the result for the best fit reconstruction while magenta lines represent the  
 1098 results for the individual scenarios from the top panel (lifetime kept constant at  $123_{-19}^{+29}$  a) as  
 1099 used in the main paper.

1100